View Article Online
View Journal

Dalton Transactions

An international journal of inorganic chemistry

Accepted Manuscript

This article can be cited before page numbers have been issued, to do this please use: M. Molla, A. Ghosh, S. G. Ghora and S. Mandal, *Dalton Trans.*, 2026, DOI: 10.1039/D6DT00632A.

ROYAL SOCIETY OF CHEMISTRY

rsc.li/dalton

View Article Online
DOI: 10.1039/D6DT00632A

ARTICLE

Copper(II) complexes for electrocatalytic dioxygen reduction: controlling selectivity via proton relay mode

Received 00th January 20xx,
Accepted 00th January 20xx

DOI: 10.1039/x0xx00000x

Mofijul Molla,[a] Ayyan Ghosh,[a] Santanu Ghora,[b] and Sukanta Mandal*[a]

Two mononuclear Cu(II) complexes, $[Cu(L_1)]^+$ (**1**$^+$) and $[Cu(L_2)(H_2O)]^+$ (**2**$^+$), were synthesized as molecular electrocatalysts for the oxygen reduction reaction (ORR). Ligand L_1^- provides an N_5-donor framework, whereas L_2^- furnishes an N_4-coordination environment; both incorporate a redox-active *N*-carboxyamidoquinolate unit that functions as a local proton reservoir and electron storage site during catalysis. Electrochemical studies at pH 7 reveal markedly different ORR selectivity for the two complexes. The N_5-ligated complex **1**$^+$ preferentially catalyzes the $4e^-/4H^+$ reduction of O_2 to H_2O with pH-independent rates and a negligible solvent kinetic isotope effect (KIE = 1.05). Computational study identifies a strong intramolecular hydrogen bond between the protonated amide N-H group and the distal oxygen atom of a putative Cu(I)-OOH intermediate, which promotes internal proton delivery and facilitates reductive O-O bond cleavage to produce H_2O. In contrast, the N_4-ligated complex **2**$^+$ predominantly catalyzes the $2e^-/2H^+$ reduction of O_2 to H_2O_2, displaying pronounced pH-dependent ORR behaviour and a larger solvent KIE (2.24), consistent with a rate-limiting external protonation step. Computational analysis reveals an unfavourable geometry for internal proton transfer in the $2e^-/H^+$ reduced form of the Cu(II)-OOH intermediate derived from **2**$^+$, accounting for its preference for partial oxygen reduction. These results, therefore, highlight how proton-relay pathways (internal *vs*. external) control product selectivity in oxygen reduction reactions.

Introduction

The oxygen reduction reaction (ORR) is an important electrochemical process that occurs in fuel cell devices.[1-3] These devices generate electrical energy by combining oxygen reduction with fuel oxidation in an electrochemical cell. For efficient fuel-to-energy conversion, the ORR must proceed at a high rate and with high energy efficiency. The ORR occurs *via* two primary routes, governed by distinct mechanistic processes and thermodynamic factors. In protic environments, O_2 can be reduced *via* either a two-electron/two-proton ($2e^-/2H^+$) mechanism, producing hydrogen peroxide (H_2O_2), or a four-electron/four-proton ($4e^-/4H^+$) pathway that directly forms water. The $4e^-/4H^+$ process may also occur in two sequential $2e^-/2H^+$ steps, in which H_2O_2 is first formed and then reduced to H_2O.

$$O_2 + 2e^- + 2H^+ \rightleftharpoons H_2O_2 \quad + 0.289\ V\ vs.\ NHE,\ at\ pH\ 7$$

$$O_2 + 4e^- + 4H^+ \rightleftharpoons 2H_2O \quad + 0.815\ V\ vs.\ NHE,\ at\ pH\ 7$$

$$H_2O_2 + 2e^- + 2H^+ \rightleftharpoons 2H_2O \quad + 1.349\ V\ vs.\ NHE,\ at\ pH\ 7$$

The direct $4e^-/4H^+$ reduction of molecular oxygen to water ($O_2 + 4H^+ + 4e^- \rightarrow 2H_2O$) has attracted significant attention due to its high thermodynamic efficiency and superior energy conversion performance without producing reactive oxygen species (ROS). This pathway is especially critical in fuel cell applications, where oxygen reduction is often the rate-limiting step at the cathode.

Platinum and its alloys have dominated the field of ORR electrocatalysis,[4] demonstrating high activity and selectivity toward the desired four-electron reduction pathway. However, the widespread implementation of platinum-based technologies faces significant economic challenges due to the metal's scarcity and high cost. Extensive research has been conducted to develop alternative catalysts based on earth-abundant 3d transition metal ions.[3,5-67] The partially filled d-orbitals of these 3d metal ions allow them to form coordinative bonds with oxygen molecules and facilitate electron transfer. Additionally, their ability to exist in multiple oxidation states enhances their catalytic versatility.

Understanding the mechanistic aspects of oxygen reduction is crucial to advancing energy conversion. One key research topic is determining the factors that control the selectivity between the $2e^-/2H^+$ and $4e^-/4H^+$ reduction pathways. In biology, heme/copper oxidases, such as *cytochrome c oxidase* (CcO), efficiently catalyze the selective reduction of O_2 to H_2O during the final stages of respiration.[68,69] Similarly, the multicopper oxidase *laccase* catalyzes the $4e^-/4H^+$ reduction of O_2 at near thermodynamic potential with high efficiency.[70,71] These natural systems inspire researchers to develop synthetic catalysts that mimic enzymatic functions.

Significant progress has been achieved in heterogeneous ORR catalysis, where metal complexes are grafted onto graphene,[9-11]

[a] *Bio-inspired Coordination Chemistry & Catalysis Laboratory, Department of Chemistry, Indian Institute of Technology Kharagpur, Kharagpur 721 302, West Bengal, India. E-mail: sukanta.mandal@chem.iitkgp.ac.in*
[b] *Functional Materials and Electrochemistry Laboratory, Department of Chemistry, Indian Institute of Technology Kharagpur, Kharagpur 721 302, West Bengal, India.*
†Electronic supplementary information (ESI) available. CCDC 2454093 (**1(PF$_6$)**), and 2454094 (**2b**). For ESI and crystallographic data in CIF or other electronic format see DOI: https:// doi.org/xxx

carbon nanotubes,[12-16] and metal-organic frameworks.[17] The ORR in a homogeneous system catalyzed by molecular catalysts is particularly intriguing due to the ease of elucidating reaction mechanisms and understanding the design principle of efficient ORR catalysts. Most research in homogeneous catalysis has focused on macrocyclic ring-based complexes inspired by the heme systems in natural enzymes.[18-38] Recently, attention has also turned to non-heme complexes, which represent a growing area of interest as potential ORR catalysts.

In recent literature, certain non-heme 3d transition-metal ion complexes (M = Mn,[39-41] Fe,[42-45] Co,[46-50] Ni,[51,52] Cu[53-67]) have been reported to exhibit chemical and/or electrocatalytic reduction of O_2. Among these, Cu-based complexes have emerged as promising ORR catalysts. One notable example is a Cu(II) complex derived from the N_4-donor ligand tris(2-pyridylmethyl)amine (tmpa) (**Cu-tmpa**). Karlin, Fukuzumi, and coworkers demonstrated that this complex efficiently and selectively catalyzes the $4e^-/4H^+$ reduction of O_2 by ferrocene derivatives in the presence of $HClO_4$ in acetone.[53] Mechanistic studies revealed that the reaction proceeds *via* the formation of a dinuclear "Cu^{II}-OO-Cu^{II}" intermediate, with no detectable formation of H_2O_2 during the chemical reduction process. Later, Hetterscheid *et al*. explored the electrochemical ORR reactivity of the **Cu-tmpa** complex in neutral aqueous solutions.[60] They observed a rapid $4e^-/4H^+$ reduction of O_2, achieving a remarkably high turnover frequency ($1.5 \times 10^5\ s^{-1}$). Under electrochemical conditions, however, the reduction proceeds *via* a stepwise $2e^- + 2e^-$ mechanism at a single copper center, producing significant amounts of H_2O_2, which are subsequently reduced to H_2O during catalysis. This observation underscores that the O_2 reduction mechanism may vary under chemical and electrochemical conditions, depending on the electron-delivery method. Further advancements by Karlin, Fukuzumi, and coworkers involved modifying the tmpa ligand by introducing a pivalamido group to one of its pyridyl arms, producing the **Cu-PV-tmpa** complex.[56] This modification significantly enhanced the catalytic performance compared to **Cu-tmpa**, highlighting the influence of ligand design on catalyst efficiency. One reason the **Cu-tmpa** complex and its derivatives exhibit efficient ORR catalysis is the flexibility of the tmpa ligand, enabling easy structural reorganizations between tetrahedral Cu(I) and non-tetrahedral Cu(II) configurations. Hetterscheid *et al.* demonstrated that ligand denticity and flexibility can influence the ORR activity and product selectivity of copper complexes.[61] The rigid **Cu-terpy** (terpy = 2,2′:6′,2″-terpyridine) and relatively less rigid **Cu-bmpa** (bmpa = bis(2-pyridylmethyl)amine) complexes, which feature N_3-donor ligands, exhibited poor $4e^-/4H^+$ ORR activity in comparison to the flexible **Cu-tmpa** complex.[61] The reduced catalytic performance of these complexes was attributed to their inability to quickly adopt the preferred tetrahedral geometry for Cu(I), leading to slower electron transfer and decreased formation of active ORR catalysts. Nevertheless, both **Cu-terpy** and **Cu-bmpa** complexes demonstrated high selectivity for the two-electron reduction of O_2 to H_2O_2.

Recent studies have highlighted the importance of the second coordination sphere in modulating ORR selectivity.[45,49,58] For instance, Kojima's work demonstrated that a mononuclear copper(II) complex with a pendant non-chelating pyridyl moiety as a proton acceptor exhibited an enhanced four-electron reduction of O_2 in acidic aqueous solutions compared to a similar complex lacking the pendant group.[58] This finding emphasizes the critical role of proton relay mechanisms facilitated by strategically positioned functional groups for improving catalytic efficiency. Furthermore, the redox-non-innocent character of the ligand framework was found to play a crucial role in storing electrons during O_2 reduction. In this context, Biswas and coworkers' investigation of a mononuclear Cu(II) complex derived from the dpaq ligand (Hdpaq = 2-[bis(pyridine-2-ylmethyl)]amino-*N*-quinolin-8-yl-acetamidate) is particularly noteworthy.[62] The dpaq ligand features a redox-non-innocent property, and the carboxamido unit acts as a proton port. It was observed that integrating proton-relay capabilities with redox-non-innocent properties synergistically enhanced proton and electron transfer processes and facilitated the reduction of O_2 to H_2O *via* the $2e^- + 2e^-$ pathway. All these research outcomes provide valuable insights into the key factors influencing ORR catalysis and suggest promising directions for future catalyst development. Investigating ORR catalysis and identifying the critical parameters that control electron-proton transfer and product selectivity between H_2O_2 and H_2O formation continue to fascinate researchers, inspiring us to pursue further studies.

Herein, we report the preparation of two new mononuclear Cu(II) complexes, $[Cu(L_1)]^+$ (**1**$^+$) and $[Cu(L_2)(H_2O)]^+$ (**2**$^+$), with ligands L_1^- {HL_1 = 2-(methyl(2-(methyl(pyridin-2-ylmethyl)amino)ethyl)amino)-*N*-(quinolin-8-yl)acetamide} and L_2^- {HL_2 = 2-((2-(benzyl(methyl)amino)ethyl)(methyl)amino)-*N*-(quinolin-8-yl)acetamide}, respectively, as potential ORR electrocatalysts (Figure 1). The ligand L_1^- serves as a penta-dentate chelating ligand, providing N_5-donor sites. We reduced the denticity of ligand HL_1 by replacing its pyridyl-benzylic moiety (-CH_2Py) with a benzylic group (-CH_2Ph) and created the ligand HL_2 with N_4-donor centers. Both ligands contain a redox-active *N*-carboxyamidoquinolate moiety. As described by Biswas *et al.*,[62] this moiety facilitates proton shuttling and electron storage, which are crucial for ORR processes. Electrochemical studies revealed that both Cu(II) complexes exhibit catalytic O_2 reduction activity in neutral aqueous solutions, with a significant difference in product selectivity. At an onset potential of 0.39 V *vs.* RHE, complex **1**$^+$ catalyzed the nearly quantitative $4e^-/4H^+$ reduction of O_2 to water, with only 14% H_2O_2 formation. Achieving this direct $4e^-/4H^+$ reduction of O_2 to water at a single copper site is noteworthy. In contrast, complex **2**$^+$ exhibited higher selectivity for the $2e^-/2H^+$ reduction of O_2, producing 85% H_2O_2 at an onset potential of 0.25 V *vs.* RHE. This difference in O_2 reduction selectivity is attributed to ligand denticity, which controls the internal proton transfer process by adjusting the position of the proton relay site relative to the "Cu-OOH" center.

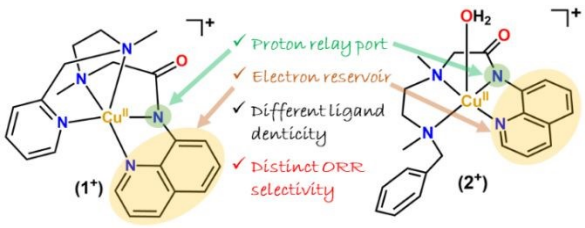

Figure 1. ChemDraw representations of Cu(II) complexes **1**$^+$ and **2**$^+$.

Results and Discussion

Synthesis and characterization. Figure S1 illustrates the synthetic protocol for preparing the ligands HL_1 and HL_2. Both ligands were characterized by ESI(+)-MS, ATR-FTIR, and NMR (^{1}H & ^{13}C) studies (see Experimental Section and Figures S2-S13). Using these ligands, we synthesized two mononuclear Cu(II) complexes, $[Cu^{II}(L_1)](ClO_4)$ (**1(ClO$_4$)**) and $[Cu^{II}(L_2)(MeOH)](ClO_4)$ (**2a(ClO$_4$)**). Both complexes were thoroughly characterized by elemental analysis, thermogravimetry, mass spectrometry, and various spectroscopic techniques. A metathesis reaction between complex **1(ClO$_4$)** and KPF_6 produced $[Cu^{II}(L_1)](PF_6)$ (**1(PF$_6$)**), which was characterized by X-ray crystallography (*vide infra*). We prepared an additional compound $[Cu^{II}(L_2)(\kappa\text{-NCS})]$ (**2b**) by reacting **2a(ClO$_4$)** with NaNCS for structural analysis (*vide infra*).

The ESI(+)-MS analysis of complexes **1(ClO$_4$)** and **2a(ClO$_4$)** in methanol revealed major peaks at *m/z* 425.1 and 424.1, corresponding to $[Cu(L_1)]^+$ and $[Cu(L_2)]^+$ ions, respectively, validating the formation of mononuclear complexes (Figures S14 and S15). The TGA curve of **2a(ClO$_4$)** exhibited an initial 5.7% weight loss at a temperature range of 50-130°C due to the loss of the coordinated methanol (Figure S16b). However, such weight loss was absent in the TGA curve for **1(ClO$_4$)**, indicating the absence of solvent molecules in the complex structure (Figure S16a). These observations are consistent with the molecular formula of the complexes: $[Cu^{II}(L_1)](ClO_4)$ (**1(ClO$_4$)**) and $[Cu^{II}(L_2)(MeOH)](ClO_4)$ (**2a(ClO$_4$)**), as determined from the elemental analyses. Thus, the Cu(II) center appears to adopt a five-coordinate geometry in both complexes. In ATR-FTIR spectra, complexes **1(ClO$_4$)** and **2a(ClO$_4$)** displayed strong bands at 1624 cm^{-1} and 1601 cm^{-1}, respectively, attributed to the C=O stretch of the amide group (ν(C=O)$_{amide}$) present in ligand frameworks (Figure S17a,b). Complex **2a(ClO$_4$)** showed a broad band near 3400 cm^{-1}, assignable to methanol's ν(O-H) vibration. Both complexes exhibited $\nu(ClO_4)$ vibration bands at ~1100 and 620 cm^{-1}. Complex $[Cu^{II}(L_2)(\kappa\text{-NCS})]$ (**2b**) exhibited the ν(C=O)$_{amide}$ band at 1618 cm^{-1} and a prominent ν(CN) band at 2076 cm^{-1} for the thiocyanate group (Figure S17c).

We recorded the EPR spectra of **1(ClO$_4$)** and **2a(ClO$_4$)** complexes in methanol at 7 K under frozen conditions (Figure S18). Complex **1(ClO$_4$)** exhibited an axial EPR spectrum with $g_\parallel = 2.22$ and $g_\perp = 2.05$. The signal in the $g_\parallel$ region showed four well-resolved hyperfine lines, with an $A_\parallel$ value of approximately 538 MHz. Complex **2a(ClO$_4$)** also displayed a similar axial spectrum ($g_\parallel = 2.23$ and $g_\perp = 2.05$), with hyperfine splitting in the $g_\parallel$ region and an $A_\parallel$ value of ~ 531 MHz. These hyperfine lines originated from the interaction between the unpaired electron spin and the nuclear spin ($I = 3/2$) of the Cu(II) center. Additionally, for complex **2a(ClO$_4$)**, super-hyperfine lines were observed due to the interaction of the Cu(II) unpaired electron spin with the ^{14}N ($I = 1$) nuclear spin. The experimental spectra of both complexes were simulated using the EasySpin program,[72,73] and the fitting parameters are listed in Table S1. The axial spectral behavior ($g_\parallel > g_\perp > 2$) of both complexes suggests a square- or square pyramidal-based geometry around the Cu(II) ion, with the unpaired electron occupying the $d_{x^2-y^2}$ orbital as the ground state.[74]

The electronic spectra of **1(ClO$_4$)** and **2a(ClO$_4$)** complexes in methanol exhibited high-intensity bands at 257 and 365 nm in the UV region, attributed to charge-transfer transitions. Complex **1(ClO$_4$)** showed three low-intensity d-d bands at 975, 820, and 598 nm (Figure S19a). These bands are tentatively assigned to the transitions $^2B_1 \rightarrow {}^2A_1$, $^2B_1 \rightarrow {}^2B_2$, and $^2B_1 \rightarrow {}^2E$, respectively, characteristic of a square-pyramidal geometry (*vide infra*).[75] For complex **2a(ClO$_4$)** in methanol, the d-d bands appeared at 620 and 930 nm; however, the latter band was not well-resolved (Figure S19b). Notably, the d-d band at 620 nm was blue-shifted to 610 nm when the absorption spectrum of **2a(ClO$_4$)** was recorded in water (Figure S20). This shift can be attributed to the formation of an aqua-ligated species, $[Cu^{II}(L_2)(H_2O)]^+$ (**2$^+$**), resulting from the replacement of methanol in complex $[Cu^{II}(L_2)(MeOH]^+$.[76] Complex $[Cu^{II}(L_2)(\kappa\text{-NCS})]$ (**2b**) showed d-d bands at 632 and 970 nm in methanol (Figure S21).

To investigate the redox-non-innocent behavior of the ligands, we synthesized zinc(II) complexes, $[Zn^{II}(L_1)(MeOH)](ClO_4)$ (**3(ClO$_4$)**) and $[Zn^{II}(L_2)(MeOH)_2](ClO_4)$ (**4(ClO$_4$)**), as reference compounds. These complexes were thoroughly characterized using analytical and spectroscopic techniques (see Experimental Section and Figures S22-S29).

Structure of copper(II) complexes. We obtained single crystals of the complex $[Cu^{II}(L_1)](PF_6)$ (**1(PF$_6$)**) by slowly diffusing diethyl ether vapor into a methanol solution of the complex. Complex **1(PF$_6$)** crystallized in an orthorhombic crystal system belonging to the $Pna2_1$ space group. The X-ray diffraction study revealed a square-pyramidal geometry for **1$^+$** (Figure 2a), with an Addison[77] τ value of 0.017. The angles around the Cu(II) center deviate significantly from the ideal square pyramidal angles (Table S2), implying a distorted geometry. The four donor atoms of the L_1^- ligand, namely, the quinoline nitrogen (N1), amide nitrogen (N2), one of the tertiary amine nitrogens (N3), and pyridyl nitrogen (N5), occupy the four equatorial coordination sites. Among them, the quinoline N1 and tertiary amine N3 are *trans* to each other, as are amide N2 and pyridyl N5. The other tertiary amine nitrogen (N4) of the ligand L_1^- occupies the axial coordination site. The axial Cu-N4 bond (2.266 Å) is longer than the equatorial Cu-N distances (1.929-2.053 Å, Table S2). This axial elongation arises from the Jahn-Teller distortion, typical for a d^9 Cu(II) complex. Notably, the geometry of complex **1$^+$** differs distinctly from that of the analogous $[Cu(dpaq)]^+$ complex, which has a geometry closer to trigonal bipyramidal.[62] We optimized the structure of **1$^+$** in its doublet ground state by Density Functional Theory (DFT) methods, incorporating a water solvation model (Figure 2b). The optimized structural parameters (bond lengths and angles) closely match the crystallographic data (Table S2). A Mulliken spin density value of 0.53 was determined for the copper center, confirming its +II oxidation state in **1$^+$**. Interestingly, the spin density plot on the Cu(II) center closely resembles the shape of a $d_{x^2-y^2}$ orbital, indicating that the unpaired spin resides on the $d_{x^2-y^2}$ orbital, as expected for a square-pyramidal geometry (Figure 2c).

The crystallographic structure of the complex $[Cu^{II}(L_2)(\kappa\text{-NCS})]$ (**2b**) revealed a square-pyramidal geometry around the Cu(II) center (Figure 2d), with a τ value of 0.076. The three N-donor atoms of ligand L_2^-, *viz*., the quinoline nitrogen (N1), amide nitrogen (N2), and one tertiary amine nitrogen (N3), occupy the equatorial coordination sites. An external thiocyanate ligand occupies the fourth equatorial position. The remaining tertiary amine nitrogen (N4) of the ligand L_2^- coordinates to the copper center at the axial position, exhibiting an elongated Cu-N(4) bond distance of 2.342(2) Å (Table S3).

In the absence of a crystal structure of $[Cu^{II}(L_2)(H_2O)]^+$ (**2$^+$**), we determined its DFT-optimized structure (Figure 2e) using the *x*, *y*, and *z* coordinates of structure **2b** and replacing the thiocyanate group

View Article Online
DOI: 10.1039/D6DT00632A

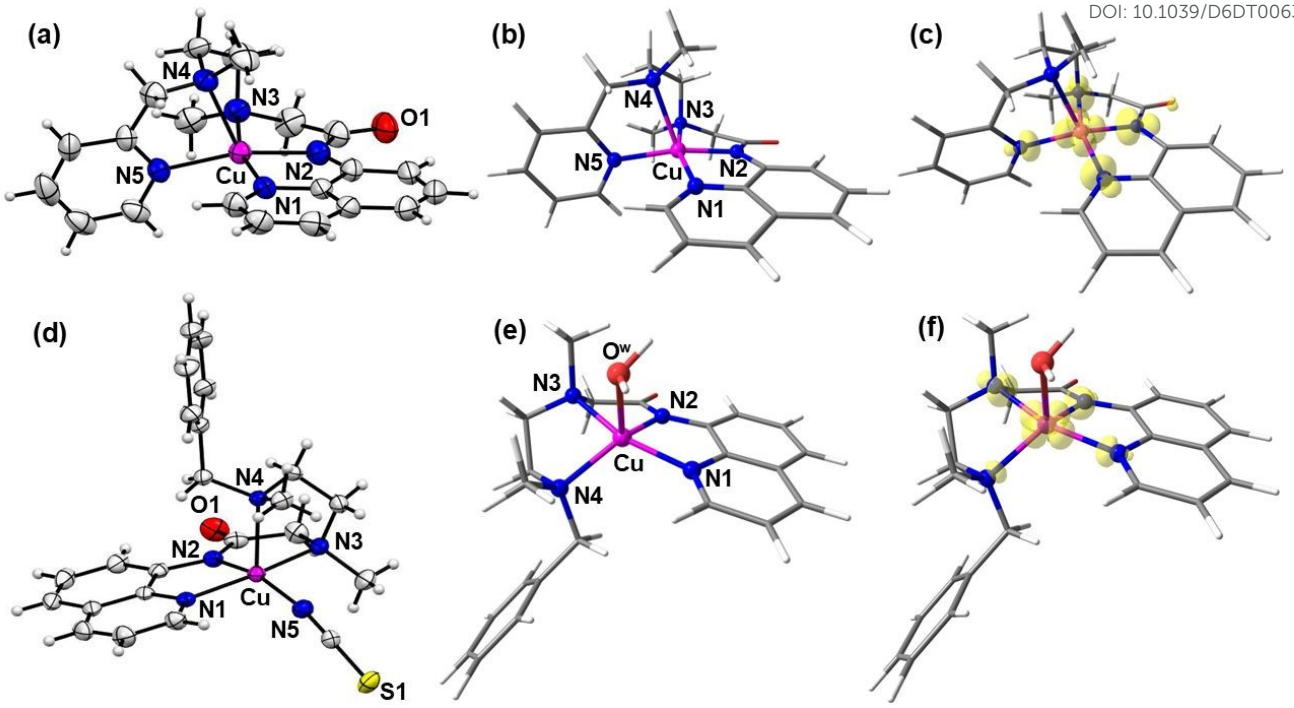

Figure 2. (a) ORTEP diagram (30% thermal ellipsoids) of the complex cation **1**$^+$ in the crystal structure of [$Cu^{II}(L_1)$](PF_6) (**1(PF$_6$)**) (counter anion is not shown), (b) DFT-optimized structure of **1**$^+$ and (c) the corresponding Mulliken spin-density plot at the doublet ground state. (d) ORTEP diagram (30% thermal ellipsoids) of complex [$Cu^{II}(L_2)$(κ-NCS)] (**2b**). (e) DFT-optimized structure of the complex [$Cu^{II}(L_2)(H_2O)]^+$ (**2**$^+$), and (f) the corresponding Mulliken spin-density plot at the doublet ground state.

with an aqua ligand. The optimized structure of **2**$^+$ in the doublet ground state exhibits a distorted square-pyramidal geometry (τ = 0.32) around the Cu(II) center, with Jahn-Teller elongation observed along the Cu-OH_2 bond (2.383 Å, Table S4). Like **1**$^+$, the Mulliken spin density plot of **2**$^+$ indicates a +II oxidation state for the copper center (Figure 2f).

Additionally, we performed frontier molecular orbital analysis of **1**$^+$ and **2**$^+$, revealing two adjacent lowest unoccupied molecular orbitals (LUMOs) separated by a narrow energy gap in both complexes: one centered on the Cu(II) (β-LUMO) and the other on the quinoline (α-LUMO+1), as shown in Figure S30. These orbitals are likely to be involved in accommodating electrons during the reduction of **1**$^+$ and **2**$^+$ (*vide infra*).

Stability of the copper(II) complexes in buffer solutions. Before investigating the electrocatalytic ORR activity of complexes **1**$^+$ and **2**$^+$, we first evaluated their stability in aqueous phosphate buffer using mass spectrometry, EPR, and UV-vis spectroscopy. The ESI(+)-MS spectra of the complexes in pH 7 phosphate buffer (Figures S31-S32) displayed intense signals at *m/z* 425.1 and 424.1, corresponding to [$Cu(L_1)]^+$ and [$Cu(L_2)]^+$, respectively. These results are consistent with those observed in methanol solution (Figures S14-S15), indicating that the ligand-bound Cu complexes remain stable in aqueous phosphate buffer.

Further evidence for the stability of the complexes was obtained from EPR spectroscopy. The EPR spectra of **1**$^+$ and **2**$^+$, recorded at 2 mM concentration in a 70% aqueous phosphate buffer and 30% MeOH mixture at 77 K, exhibited axial spectral features similar to those observed in frozen MeOH (Figure S33). To determine whether these spectral features of **1**$^+$ and **2**$^+$ originate from ligand-bound Cu species or from free Cu^{2+} ions, we recorded the EPR spectrum of copper(II) acetate in the same solvent mixture. However, the copper(II) acetate sample (~2 mM) in phosphate buffer produced a precipitate, likely due to the formation of copper phosphate, and showed weak EPR signals (Figure S34). To avoid this precipitation, the EPR spectrum of copper(II) acetate was measured in a 70% non-buffered water/30% MeOH mixture at 77 K. Under this condition, it exhibited an axial EPR spectrum (Figure S35), suggesting the dissociation of its dimeric form to a monomer in aqueous medium.[78] The spectra of **1**$^+$ and **2**$^+$ were also measured under identical non-buffered conditions for comparison. Notably, $Cu(OAc)_2$ displayed a higher $g_{\|}$ value (2.33) than complexes **1**$^+$ (2.22) and **2**$^+$ (2.23). This observation indicates that the metal-ligand interactions in $Cu(OAc)_2$ are predominantly ionic in nature, whereas those in complexes **1**$^+$ and **2**$^+$ are more covalent.[66,79] These spectral differences, therefore, clearly demonstrate that the coordination environments of the Cu^{2+} ions in complexes **1**$^+$ and **2**$^+$ differ from that of $Cu(OAc)_2$ in aqueous solution, establishing that the EPR signals for **1**$^+$ and **2**$^+$ originate from the ligand-stabilized Cu^{2+} centers rather than free Cu^{2+} species.

Furthermore, we recorded electronic spectra of **1**$^+$ and **2**$^+$ in both phosphate-buffered and non-buffered aqueous solutions. In both media, the d-d band positions of the respective copper complexes remained nearly identical, indicating that the phosphate anions did not coordinate to the Cu(II) centers. In contrast, $Cu(OAc)_2$ in non-buffered water exhibited a weak d-d band at ~770 nm, which is distinctly different from those observed for **1**$^+$ (595 nm) and **2**$^+$ (610 nm) (Figure S36).

Taken together, these controlled experiments demonstrate that complexes **1**$^+$ and **2**$^+$ retain their ligand-bound coordination

View Article Online
DOI: 10.1039/D6DT00632A

structures in both phosphate-buffered and non-buffered aqueous solutions.

Electrochemical study. To explore the redox properties of complexes $\mathbf{1}^+$ and $\mathbf{2}^+$, we conducted cyclic voltammetry (CV) and differential pulse voltammetry (DPV) measurements in a pH 7 aqueous 0.1 M phosphate buffer at room temperature under a dinitrogen atmosphere (Figure 3 and Figure S37, respectively). Complex $\mathbf{1}^+$ showed a quasi-reversible cyclic voltammogram at $E_{1/2}$ = -0.076 V *vs.* RHE, with a peak-to-peak separation of 168 mV. In contrast, complex $\mathbf{2}^+$ exhibited an irreversible reduction wave at E_{pc} = -0.140 V *vs.* RHE. The $E_{1/2}$ for $\mathbf{2}^+$ was determined to be 0.114 V *vs*. RHE by DPV, which is more anodic than the $E_{1/2}$ for $\mathbf{1}^+$. Furthermore, the CV of a suspension of $Cu(OAc)_2$ in phosphate buffer (pH 7) under N_2 displayed a featureless profile, except for a small redox wave at 0.56 V *vs*. RHE, likely arising from the deposition of copper phosphate on the electrode surface (Figure 3). This finding confirms that the redox responses of $\mathbf{1}^+$ and $\mathbf{2}^+$ arise from ligand-bound copper species rather than free Cu^{2+} ions or electrode deposits, further establishing the molecular integrity of both copper complexes in phosphate buffer.

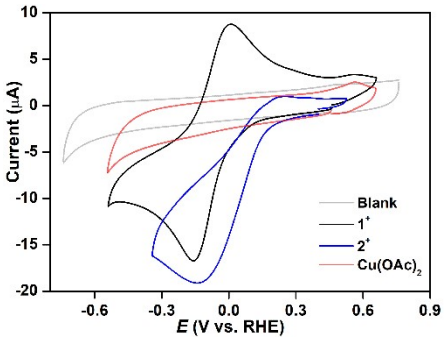

Figure 3. CVs of complexes $\mathbf{1}^+$ (black), $\mathbf{2}^+$ (blue), and $Cu(OAc)_2$ (red) in a pH 7 aqueous 0.1 M phosphate buffer under an inert N_2 atmosphere ([complex] ~ 1 mM; scan rate = 100 mV/s). The gray line represents a blank CV under identical conditions.

In the CV diagrams, the relatively large peak-to-peak separation for $\mathbf{1}^+$ and the irreversible nature of the CV response for $\mathbf{2}^+$ suggest significant structural rearrangement during reduction, tentatively converting from a square-pyramidal to a (pseudo)trigonal geometry (*vide infra*). Notably, the structural rearrangement in $\mathbf{2}^+$ appears slower than in $\mathbf{1}^+$ on the CV time scale, resulting in an irreversible voltammogram for $\mathbf{2}^+$. Measuring the CV of $\mathbf{2}^+$ at a very high scan rate (*e.g.,* 5 V/s) also produced an irreversible response. The irreversibility observed for $\mathbf{2}^+$ might also indicate that the complex breaks down during reduction, potentially releasing Cu(I) ions into solution. However, no CV features due to deposited metallic copper on the electrode surface, expected from Cu(I) disproportionation, were observed under inert conditions. In addition, a rinse test with $\mathbf{2}^+$ confirmed the absence of deposited material on the electrode surface under nitrogen (Figure S38). These findings demonstrate that complex $\mathbf{2}^+$ was stable during cathodic scans, attesting that the irreversible CV behavior of $\mathbf{2}^+$ was due to slower structural rearrangements, a phenomenon commonly observed for copper complexes. For both complexes, the peak currents show linear correlations with the square root of the scan rates, indicating diffusion-controlled homogeneous behavior near the electrode and negligible deposition of the complexes on the electrode surface (Figures S39 and S40).

Furthermore, we performed electrochemical studies of both $\mathbf{1}^+$ and $\mathbf{2}^+$ complexes over a pH range of 3 to 9 to clarify the electro-reduction processes. The Pourbaix diagrams revealed that the reduction processes were pH-dependent for both complexes, decreasing linearly with a slope close to -30 mV/pH (Figures S41 and S42). These trends suggest a $2e^-/1H^+$ proton-coupled electron transfer (PCET) process. We tentatively attributed these redox events to the reduction of Cu^{II} to Cu^{I}, accompanied by a ligand-centered proton-coupled reduction. A similar mixed metal-ligand-based $2e^-/1H^+$ reduction was previously observed in the $[Cu^{II}(dpaq)]^+$ complex reported by Biswas *et al*.[62]

To assess the redox-non-innocent nature of the ligands L_1^- and L_2^-, we conducted CV studies on their corresponding zinc(II) complexes, $[Zn^{II}(L_1)(MeOH)]^+$ ($\mathbf{3}^+$) and $[Zn^{II}(L_2)(MeOH)_2]^+$ ($\mathbf{4}^+$), under pH 7 conditions. Both Zn(II) complexes showed electrochemical activity during a cathodic scan, displaying irreversible reductive waves at $E_{1/2}$ = -0.60 V *vs.* RHE for $\mathbf{3}^+$ and $E_{1/2}$ = -0.65 V *vs*. RHE for $\mathbf{4}^+$ (Figure S43). Interestingly, these reduction processes were pH-sensitive, as indicated by the Pourbaix diagram (Figure S44), which showed a slope of nearly -59 mV/pH, consistent with a $1e^-/1H^+$ PCET process. The free ligands also displayed cathodic reduction waves, similar to those of their Zn(II) complexes. By comparing the electrochemical behavior of the Cu(II) and Zn(II) complexes, we confirm that the reduction mechanism in $\mathbf{1}^+$ and $\mathbf{2}^+$ involves two-centered processes: one centered on the Cu(II) and another based on the ligand. These findings highlight the ability of the Cu(II) center and its coordinated ligand to store electrons and protons, which may facilitate oxygen reduction reactions.

We performed DFT calculations to get deeper insights into the nature of the $2e^-/1H^+$ reduced species of $\mathbf{1}^+$ and $\mathbf{2}^+$. Among the two most likely protonation sites, anionic amidate-N and -O, protonation at the amidate-N generated the most stable reduced form in both cases. The DFT-optimized structures of the $2e^-/1H^+$-reduced forms of $\mathbf{1}^+$ and $\mathbf{2}^+$ in their doublet ground states reveal distorted trigonal-planar and trigonal-mono-pyramidal geometries, respectively, around the copper center (Figures S45a,c). Spin density plots indicate a Cu(I) state in both reduced species, with the unpaired spin mostly delocalized over the quinoline moiety (Figures S45b,d). These calculations, therefore, indicate that during the $2e^-$ reduction, the Cu(II) center accepts one electron to form Cu(I), and the second electron occupies a quinoline-based orbital. This interpretation is in good agreement with the frontier molecular orbital analysis of $\mathbf{1}^+$ and $\mathbf{2}^+$ discussed above.

Electrocatalytic O_2 reduction by the Cu(II) complexes. We investigated the electrocatalytic ORR reactivity of $\mathbf{1}^+$ and $\mathbf{2}^+$ in an oxygen-saturated 0.1 M aqueous phosphate buffer (pH 7) at room temperature. The cyclic voltammograms of both complexes displayed distinct catalytic currents in the presence of dioxygen, as shown in Figure 4. Complex $\mathbf{1}^+$ exhibited the catalytic wave with an onset potential of 0.39 V *vs*. RHE, while complex $\mathbf{2}^+$ showed the catalytic wave initiating at 0.25 V *vs*. RHE, which are cathodically shifted as compared to the onset potential of **Cu-tmpa** and $[Cu(dpaq)]^+$ complexes (*e.g.*, +0.50 V *vs*. RHE).[60,62] The catalytic waves due to oxygen reduction by $\mathbf{1}^+$ and $\mathbf{2}^+$ displayed well-defined peak shapes, indicating controlled electron transfer processes. The control

View Article Online
DOI: 10.1039/D6DT00638A

experiment with a bare GC electrode (without complex) also exhibited an oxygen reduction current (Figure 4). However, the electrocatalytic current at the bare electrode was much lower than that of both complexes. Moreover, the bare GC electrode showed ORR at a more negative onset potential than the copper complexes. These findings confirm the effectiveness of the present copper complexes in electrocatalytic oxygen reduction reactions. Comparative CVs of complexes $\mathbf{1}^+$ and $\mathbf{2}^+$ in oxygen-saturated and nitrogen atmospheres revealed that the $2e^-/H^+$-reduced forms of both complexes trigger electrocatalytic oxygen reduction. We observed that the half-wave potential of the catalytic wave ($E_{cat/2}$) is greater than $E_{1/2}$ (particularly for $\mathbf{1}^+$), likely due to substrate depletion near the electrode.[60] In both systems, the electrocatalytic current demonstrated a linear first-order correlation with the catalyst concentrations (Figures S46-S47), indicating the homogeneous nature and the involvement of a single Cu-complex during ORR.[60,62]

Figure 4. CV diagrams of complexes (a) $\mathbf{1}^+$ and (b) $\mathbf{2}^+$ in the presence (red line) and absence of O_2 (black line) ([complex] ~ 1 mM; scan rate = 100 mV/s; pH 7, 0.1 M phosphate buffer). The gray lines correspond

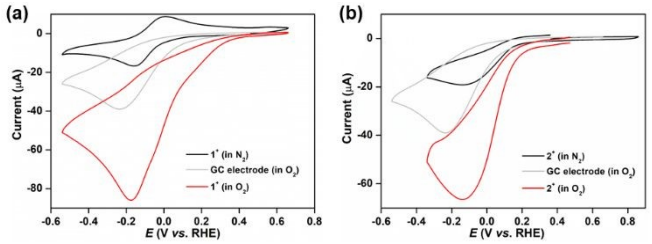

to the oxygen-saturated pH 7 phosphate buffer CVs with a bare GC electrode (without complex).

We conducted rinse tests to further investigate whether the observed ORR activity originated from molecular copper complexes in solution or from small deposits on the electrode surface. As shown in Figure S48, repeated CV scans resulted in a gradual decrease in the catalytic currents for both Cu(II)-complexes, reaching a stable value after ~9 consecutive ORR cycles. For both complexes, a new, however small, redox wave at around 0.56 V *vs*. RHE appeared during consecutive scans. This new redox peak is associated with the formation of a polymeric copper phosphate deposit on the electrode surface, as previously reported for other copper complexes in phosphate buffer during ORR.[64,65] However, rinse-test experiments with the unpolished GC electrode bearing the tiny deposited materials showed no significant electrocatalytic ORR activity during CV measurements in catalyst-free, oxygen-saturated phosphate buffer (Figure S49). The catalytic peak current observed for the rinsed GC electrode was nearly the same as that of the freshly polished GC electrode under the same conditions. These results demonstrate that the deposited Cu-phosphate species did not contribute to the observed ORR activity. Moreover, the CV of $Cu(OAc)_2$ recorded under identical conditions in oxygen-saturated phosphate buffer exhibited considerably smaller catalytic currents than those observed for $\mathbf{1}^+$ and $\mathbf{2}^+$ (Figure S50), supporting that the ORR activity of $\mathbf{1}^+$ and $\mathbf{2}^+$ originated from the ligand-bound Cu complexes rather than from free Cu^{2+} ions.[66]

Additionally, we assessed the stability of the complexes during ORR by controlled-potential electrolysis in oxygen-saturated pH 7 phosphate buffer, with an FTO (~1.5 cm^2) as the working electrode (Figures S51a and S52a). The applied potential was set to the corresponding $E_{cat/2}$ value of the complexes: 0.007 V for $\mathbf{1}^+$ and 0.057 V for $\mathbf{2}^+$ *vs*. RHE. The electrolysis was conducted for 1 hour, during which a constant current was maintained for both complexes, indicating that they retained their electrocatalytic performance for the entire duration of the experiment. Electronic spectra, recorded before and after electrolysis, showed a slight decrease (~5% for $\mathbf{1}^+$ and ~10% for $\mathbf{2}^+$) in the absorbance of the d-d bands for both complexes (Figures S51b and S52b). These results suggest that the complexes largely maintained their molecular integrity, although they underwent minor decomposition under long-term electrocatalytic conditions. We examined the post-catalysis FTO electrodes using scanning electron microscopy (SEM), energy-dispersive spectroscopy (EDS), and X-ray photoelectron spectroscopy (XPS) to investigate the nature of the decomposition products (Figures S53-S55). SEM imaging revealed a deposited layer on the electrode surface in both cases. EDS analysis detected copper in the deposited substances, whereas phosphorus was detected only at trace levels, indicating nominal deposition of copper phosphate on the electrode surface. Analysis of the high-resolution Cu 2p XPS spectra revealed both metallic Cu(0) and Cu(II) species in the deposited layer. These results suggest that during the electrocatalytic oxygen reduction process, a fraction of the Cu(I) intermediates undergoes decomposition followed by disproportionation to form Cu(0) and Cu(II), which may represent a potential deactivation pathway for the complexes under prolonged electrolytic conditions.

We performed rotating ring-disk electrode (RRDE) voltammetry to determine the number of electrons transferred and the product distribution (H_2O_2 *vs*. H_2O) during O_2 reduction by complexes $\mathbf{1}^+$ and $\mathbf{2}^+$ at pH 7 (Figure 5). The RRDE setup employed a glassy carbon disk electrode, which was scanned over a potential window of 0.80 V to -0.27 V *vs*. RHE for $\mathbf{1}^+$ and 0.80 V to -0.50 V *vs*. RHE for $\mathbf{2}^+$, coupled with a platinum ring electrode held at 1.4 V *vs*. RHE. This ring potential was selected to oxidize any H_2O_2 generated, which was hydrodynamically transported to the ring during the electrocatalytic ORR process. Thus, simultaneous measurement of the ring and disk currents enabled us to quantitatively analyze the reaction products. The percentage of generated H_2O_2 and the total number of electrons transferred (n) were determined using equations (1) and (2), respectively, with a collection efficiency (N) of 0.25 (Supporting Information).[60,62,80] Complex $\mathbf{1}^+$ produced around 14% H_2O_2 during electrochemical oxygen reduction catalysis, with an n value of 3.71 at an onset potential of 0.39 V *vs*. RHE. In contrast, complex $\mathbf{2}^+$ generated approximately 85% H_2O_2 during electrochemical ORR, with an n value of 2.30 at an onset potential of 0.25 V *vs*. RHE. The formation of H_2O_2 during ORR catalyzed by complex $\mathbf{2}^+$ was further confirmed by iodometric measurements (Figure S56), which showed ~60% H_2O_2 during controlled-potential electrolysis at an applied potential of 0.057 V *vs.* RHE at pH 7. Notably, the bare GC electrode and $Cu(OAc)_2$ exhibited distinct RRDE voltammograms with more negative ORR onset potentials than $\mathbf{1}^+$ and $\mathbf{2}^+$ (Figure S57). These findings again confirm that the observed ORR activity arises primarily from the molecular Cu(II) complexes in solution rather than from free Cu^{2+} ions or heterogeneous materials.

View Article Online
DOI: 10.1039/D6DT00632A

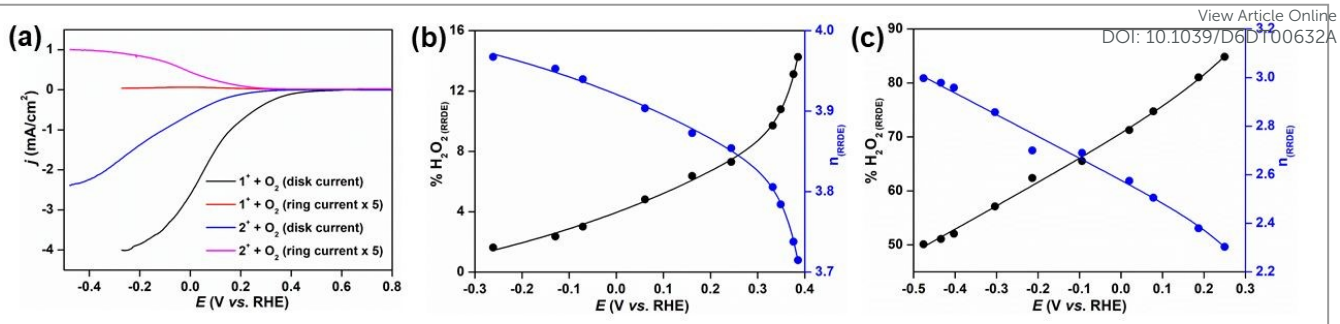

Figure 5. (a) RRDE data of complexes **1**$^+$ and **2**$^+$ under oxygen in a 0.1 M pH 7 phosphate buffer. (b) Amount of %H_2O_2 and number of electrons (n_{RRDE}) calculated from RRDE chronoamperometry measurements with complex **1**$^+$, and (c) corresponding with complex **2**$^+$. Conditions: [complex] = 0.1 mM; rotation speed = 900 rpm; ring potential: 1.4 V *vs*. RHE.

In the chronoamperometric measurements (Figures S58-S59), as the applied potential was shifted more cathodically relative to the onset, H_2O_2 production gradually decreased while the number of electrons transferred increased (Figure 5). For complex **1**$^+$, the H_2O_2 amount was 14% at the onset potential of 0.39 V *vs*. RHE, decreasing to 1.62% at -0.26 V *vs*. RHE, while n increased from 3.71 to 3.97 (Table S5). On the other hand, for complex **2**$^+$, H_2O_2 formation decreased from 85% at the onset potential of 0.25 V *vs*. RHE to 50% at -0.48 V *vs*. RHE, with n increasing from 2.30 to 3.00 (Table S6). These results reveal distinct electrocatalytic behaviors of complexes **1**$^+$ and **2**$^+$, particularly in their selectivity for ORR. Complex **1**$^+$ exhibited greater selectivity for the $4e^-/4H^+$ electrocatalytic reduction of dioxygen to H_2O, whereas complex **2**$^+$ showed higher selectivity in the $2e^-/2H^+$ reduction of dioxygen to H_2O_2.

$$\%H_2O_2 = \frac{2 \times \left(\frac{i_{ring}}{N}\right)}{i_{disk} + \left(\frac{i_{ring}}{N}\right)} \times 100 \qquad (1)$$

$$n = \frac{4 \times i_{disk}}{i_{disk} + \left(\frac{i_{ring}}{N}\right)} \qquad (2)$$

The product H_2O_2 was formed only in minor amounts during the electrochemical reduction of O_2 by complex **1**$^+$, as revealed by chronoamperometry. This observation indicates that **1**$^+$ preferentially catalyzes the direct $4e^-/4H^+$ reduction of dioxygen to water, unlike **Cu-tmpa** and $[Cu(dpaq)]^+$, which followed a sequential $2e^- + 2e^-$ reduction mechanism under electrochemical conditions.[60,62] In contrast, for complex **2**$^+$, the H_2O_2 accumulation decreased from about 85% at the onset potential (0.25 V *vs.* RHE) to 50% at a more cathodic potential (-0.48 V *vs*. RHE), suggesting an initial rapid $2e^-$ reduction of O_2 to H_2O_2, followed by a sluggish $2e^-$ reduction of H_2O_2 to water at more negative potentials. To validate these interpretations, RDE linear sweep voltammetry (RDE-LSV) experiments were conducted at 900 rpm in the presence of H_2O_2 under argon, using complexes **1**$^+$ and **2**$^+$. The resulting catalytic currents were then compared with those obtained with O_2 and a mixture of H_2O_2 and O_2 (Figure S60). Before analyzing the results of these control experiments, we cross-checked the stability of both complexes in the presence of H_2O_2 using UV-vis spectroscopy. The d-d bands in the absorption spectra remained unaffected upon addition of H_2O_2 to aqueous phosphate buffer (pH 7) solutions of the complexes at room temperature (Figure S61), indicating that H_2O_2 neither binds with Cu(II) complexes nor undergoes disproportionation in the presence of these complexes. As shown in Figure S60a, the controlled RDE-LSV experiments with complex **1**$^+$ showed only a slight catalytic current upon addition of H_2O_2, with an onset at 0.24 V *vs*. RHE. Moreover, the current response obtained in the presence of both H_2O_2 and O_2 differed only slightly from that observed with O_2 alone. These results demonstrate that **1**$^+$ does not effectively catalyze the electrochemical reduction of H_2O_2, thereby ruling out the stepwise $2e^- + 2e^-$ pathway and supporting the direct $4e^-/4H^+$ reduction of O_2 to H_2O. On the contrary, for complex **2**$^+$, the presence of both H_2O_2 and O_2 produced a considerably enhanced catalytic current relative to O_2 alone as the potential was scanned toward more cathodic values from the onset potential (Figure S60b). This finding supports the notion that **2**$^+$ can promote the sequential $2e^- + 2e^-$ reduction of dioxygen to some extent, particularly at more negative potentials.

We further constructed Tafel plots (Figures S62 and S63) for the ORR catalyzed by complexes **1**$^+$ and **2**$^+$ by plotting the applied potential against the logarithm of the disk current density ($\log(j_k)$),[60] as obtained from RDE responses. To determine the Tafel slope values, we considered the potential range from the onset potential to the potential at which the measured disk current was not mass-transport limited. A single linear Tafel slope of -225 mV/dec was observed for complex **1**$^+$ within this potential range (Figure S62). This Tafel profile of **1**$^+$ differs from that of the **Cu-tmpa** complex reported by Hetterscheid *et al*.[60] The **Cu-tmpa** complex exhibited two distinct potential regions with different Tafel slopes, consistent with the stepwise $2e^- + 2e^-$ reduction of O_2. Therefore, the observation of a single linear Tafel slope for **1**$^+$ may suggest a different ORR mechanism from the $2e^- + 2e^-$ pathway, possibly indicating a direct $4e^-/4H^+$ reduction of O_2. However, this single linear Tafel slope for **1**$^+$ does not provide definitive evidence for the direct $4e^-/4H^+$ ORR mechanism; hence, this interpretation should be considered speculative at this stage. On the contrary, complex **2**$^+$ showed two distinct potential regions, one from 0.20 to 0.025 V and another from 0.025 to -0.14 V, with corresponding Tafel slopes of -228 mV/dec and -337 mV/dec, respectively (Figure S63). Notably, the Tafel slope for H_2O_2 reduction by **2**$^+$ under inert conditions is -322 mV/dec, which is close to the -337 mV/dec slope observed in the 0.025 to -0.14 V region during the ORR. This observation suggests that **2**$^+$ can promote the $2e^- + 2e^-$ mechanism in this potential regime, as discussed above. Nevertheless, for homogeneous molecular catalysts that involve multi-electron, multistep reactions with several

View Article Online
DOI: 10.1039/D6DT00673M

diffusing species, Tafel slope values should be interpreted with caution. Therefore, the Tafel analyses presented here provide only qualitative information.

We determined the rate constants for oxygen reduction (k_{cat}) catalyzed by **1**$^+$ and **2**$^+$ using the peak current method, as described in equation (3). In this equation, i_c represents the catalytic peak current, i_p is the peak current of the catalyst reduction in the absence of dioxygen, n_c is the number of electrons transferred at the catalytic peak potential (here, n_c = 3.96 at E_{red} = –0.180 V *vs*. RHE for **1**$^+$, and n_c = 2.59 at E_{red} = –0.138 V *vs*. RHE for **2**$^+$ in pH 7), n_p is the number of electrons transferred in non-catalytic conditions (here, n_p = 2 for both complexes), R is the gas constant (8.314 J·mol^{-1}·K^{-1}), F is the Faraday constant (96,485 C·mol^{-1}), T is the absolute temperature (298 K), and v is the scan rate. The CV experiments for the catalytic oxygen reduction by **1**$^+$ and **2**$^+$ under oxygen-saturated conditions at pH 7 were performed at different scan rates (Figure S64). From these data, the k_{cat} values were determined to be 0.80 s^{-1} and 0.033 s^{-1} at pH 7 for **1**$^+$ and **2**$^+$, respectively, based on the slope of the plots of i_c/i_p *vs*. $v^{-1/2}$, as shown in Figure 6. These k_{cat} values are higher than those reported for Kojima's Cu(II) complexes,[58] determined using the same method. The higher ORR rates observed for **1**$^+$ and **2**$^+$ compared to Kojima's complexes may come at the cost of higher overpotentials. However, the k_{cat} value for the overall 4e$^-$ reduction of O_2 by **1**$^+$ is significantly lower than that of the benchmark **Cu-tmpa**[60] complex (k_{cat} = 1.5 × 10^5 s^{-1}). Comparisons of the rate constants with [Cu(dpaq)]$^+$,[62] and other Cu-based ORR catalysts[65] could not be made, as the k_{cat} values of those reported compounds were determined using a different approach, *i.e*., the *foot-of-the-wave analysis*,[81,82] which is not appropriate for the present complexes.

$$\frac{i_c}{i_p} = \frac{n_c}{0.4463 n_p^{3/2}} \sqrt{\left(\frac{k_{cat} RT}{Fv}\right)} \qquad (3)$$

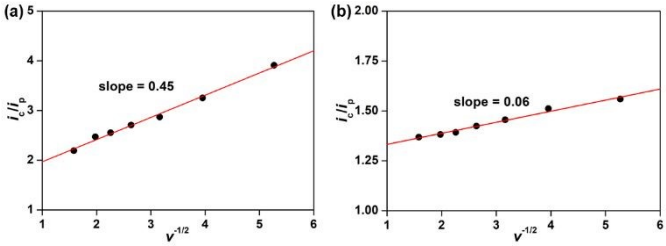

Figure 6. Plots of i_c/i_p *vs.* $v^{-1/2}$ for complexes (a) **1**$^+$ and (b) **2**$^+$. Conditions: [complex] = 1 mM, pH 7 phosphate buffer, 298 K. The background current produced by the bare GC electrode under oxygen-saturated conditions at a particular scan rate was subtracted from the corresponding i_c value.

Discussion on mechanisms. The proposed mechanisms of O_2 reduction catalyzed by **1**$^+$ and **2**$^+$ near the onset potential are depicted in Figure 7. Upon scanning towards cathodic potentials, both Cu(II) complexes, **1**$^+$ and **2**$^+$, undergo simultaneous metal- and ligand-centered 2e$^-$/H$^+$ reductions, generating the Cu(I) species [Cu^I(HL$_1$$^{\bullet-}$)] and [Cu^I(HL$_2$$^{\bullet-}$)(H$_2$O)], respectively, where the second electron is stored in the quinoline moiety and, the amidate-N atom is protonated in the corresponding ligand system as predicted from the DFT calculations. These reductions and the associated amide-N protonation result in significant structural transformation: complex **1**$^+$ converts from a square-pyramidal geometry to a trigonal planar geometry, and complex **2**$^+$ adopts a trigonal monopyramidal geometry, as revealed by the DFT-optimized structures of the respective reduced species discussed previously (Figure S45). This structural change involves the decoordination of certain donor atoms, including the protonated amide-N. These reduced copper species subsequently activate dioxygen, initiating the oxygen reduction reactions. In both catalytic reactions, O_2 reduction occurs at a single-site copper species, as previously demonstrated (Figures S46 and S47).

The O_2 molecule is initially reduced by 2e$^-$/H$^+$ during ORR to form a putative "Cu^{II}-OOH" intermediate. The formation of the Cu^{II}-OOH intermediate likely occurs through the binding of O_2 to the Cu(I) center, forming a Cu^{II}-O-O$^{\bullet-}$ superoxide species, which undergoes subsequent 1e$^-$/1H$^+$ reduction to produce the hydroperoxide species (Cu^{II}-OOH). Notably, in the later reduction step, the quinoline moiety supplies the additional electron, while the protonated pendant carboxamido group intramolecularly delivers the proton, facilitating the hydroperoxide formation. Similar reaction steps have been proposed for the O_2 reduction catalyzed by the [Cu(dpaq)]$^+$ complex.[62]

We conducted DFT calculations to gain insight into the structure of the Cu^{II}-OOH intermediates. Figure S65 presents the DFT-optimized structures and spin-density plots of [Cu^{II}(L$_1$)(OOH)] and [Cu^{II}(L$_2$)(OOH)] in their doublet ground states. In both complexes, the calculated O-O bond length is approximately 1.46 Å, ascertaining the peroxo nature of the bound dioxygen species. The optimized structure of [Cu^{II}(L$_1$)(OOH)] features a six-coordinate Cu^{II} center in a distorted octahedral geometry, with the OOH group positioned *cis* to the amide nitrogen. In contrast, the calculated structure of [Cu^{II}(L$_2$)(OOH)] exhibits a distorted square-pyramidal geometry around the Cu(II) center, with the OOH ligand occupying the equatorial site and oriented *trans* to the amide nitrogen. Our attempts to optimize [Cu^{II}(L$_2$)(OOH)] by adding an aqua ligation resulted in the water molecule remaining non-coordinated, indicating a preference for a five-coordinate geometry in this intermediate.

Experimental results (RRDE experiments) on the selectivity of the oxygen reduction reaction catalyzed by complexes **1**$^+$ and **2**$^+$ suggest that the corresponding hydroperoxide species, [Cu^{II}(L$_1$)(OOH)] and [Cu^{II}(L$_2$)(OOH)], exhibit distinct reactivity in subsequent steps (Figure 7). The [Cu^{II}(L$_1$)(OOH)] intermediate is more activated toward further PCET reduction, leading to O-O bond cleavage and predominantly producing H_2O. On the contrary, the [Cu^{II}(L$_2$)(OOH)] species is protonated at the hydroperoxo ligand, resulting in the release of H_2O_2 as the primary product near the onset potential. To elucidate these mechanistic differences, we conducted DFT calculations on the 2e$^-$/H$^+$ reduced forms of both [Cu^{II}(L$_1$)(OOH)] and [Cu^{II}(L$_2$)(OOH)] species, with protonation at the amidate-N. We emphasized these species because their formation is necessary to achieve the 4e$^-$/4H$^+$ reduction of O_2. The optimized structures and corresponding spin-density plots of both reduced hydroperoxo species are shown in Figure 8. The Mulliken spin-density analysis indicates a Cu(I) oxidation state in both species, with the unpaired electron density mainly delocalized over the quinoline moiety. Interestingly, for the 2e$^-$/H$^+$ reduced species of [Cu^{II}(L$_1$)(OOH)], *i.e*., [(HL$_1$$^{\bullet-}$)Cu^I-OOH]$^-$, the optimized structure revealed a strong intramolecular hydrogen bond

View Article Online
DOI: 10.1039/D6DT00632A

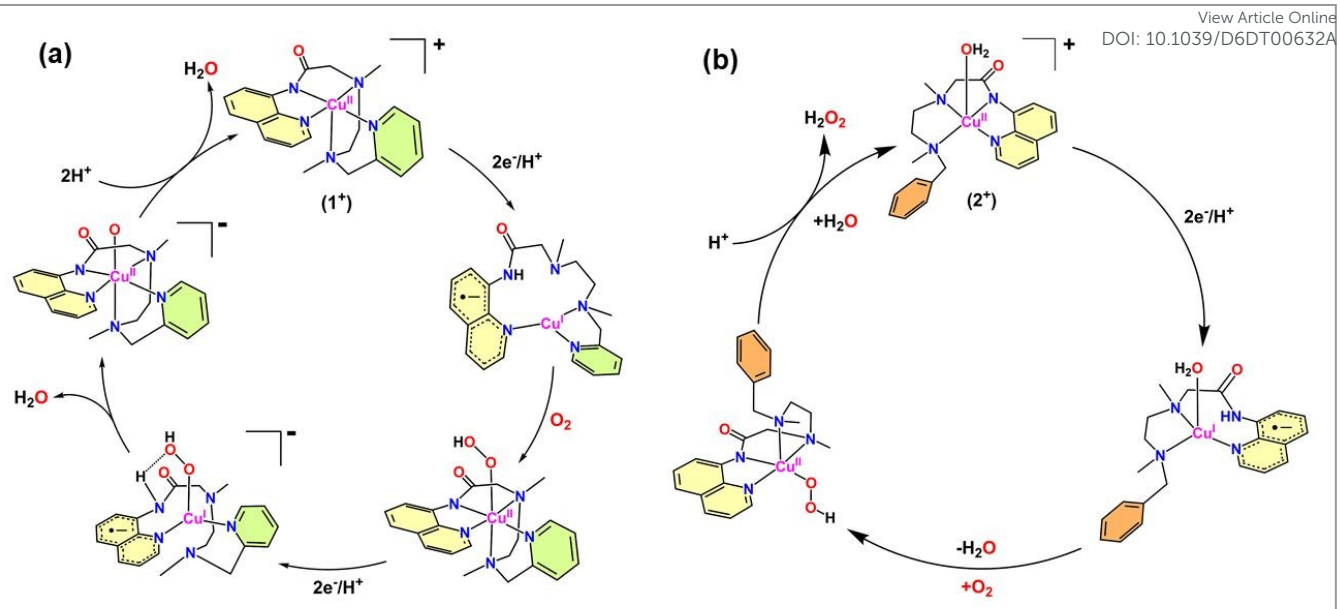

Figure 7. The proposed mechanisms of the ORR (near to the onset potentials) catalyzed by the copper(II) complexes (a) **1**$^+$ and (b) **2**$^+$.

between the pendant amide N-H and the distal oxygen of the Cu^I-OOH unit (Figure 8a). This hydrogen-bonding interaction likely facilitates an internal proton relay mechanism that assists in the reductive cleavage of O-O bond to produce H_2O (Figure 7a).[50,58] Conversely, in the $2e^-/H^+$ reduced form of $[Cu^{II}(L_2)(OOH)]$ (*i.e.* $[(HL_2^{\bullet-})Cu^{I}\text{-}OOH]^-$), the optimized structure reveals that the pendant amide N-H and the OOH group are oriented on opposite sides (Figure 8c). This opposite spatial arrangement precludes the formation of a similar intramolecular hydrogen bond as found in $[(HL_1^{\bullet-})Cu^{I}\text{-}OOH]^-$ species. As a result, further PCET reduction of the $[Cu^{II}(L_2)(OOH)]$ intermediate to yield H_2O becomes less favorable. Instead, the $[Cu^{II}(L_2)(OOH)]$ intermediate is protonated at the proximal oxygen atom of the Cu^{II}-OOH moiety by an external proton from the solvent, leading to the release of H_2O_2 (Figure 7b). Therefore, the superior performance of complex **1**$^+$ over **2**$^+$ in catalyzing the $4e^-$ reduction of O_2 stems from efficient proton transfer from the pendant amide N-H to the active Cu^I-OOH site, which facilitates reductive O-O bond cleavage, thereby enabling the $4e^-$ reduction of O_2 to proceed. Here, the protonated amide N-H functions as a local proton source, facilitating the internal proton relay mechanism analogous to the role of the tyrosine residue in the active site of *cytochrome c oxidase*.[68,69]

Elucidation of the internal and external proton relay. To rationalize the proposed internal and external proton-transfer mechanisms, we investigated the ORR activity of complexes **1**$^+$ and **2**$^+$ over a pH range of 7-9 (Figure S66). For complex **2**$^+$, an enhanced catalytic peak current was observed when the pH was changed from basic (pH 9) to neutral (pH 7) (Figure S66b). This catalytic current disappeared upon nitrogen purging, confirming that it originated solely from ORR and not from hydrogen evolution reactions. Interestingly, the k_{cat} values for ORR catalyzed by **2**$^+$ showed significant pH dependences, increasing as the pH decreased from 9 to 7. A plot of $\log(k_{cat})$ *vs*. pH showed a linear correlation with a slope value of -0.88 (Figure S67). The slope of the $\log(k_{cat})$ *vs*. pH plot[83] provides insights into the nature of the proton transfer mechanism, intermolecular *vs*. intramolecular, as demonstrated in previous studies of the hydrogen evolution reaction, where a higher slope indicates an intermolecular proton transfer from the bulk solvent to the active species, while a zero or smaller slope suggests an intramolecular proton transfer pathway.[84] In this case, the relatively large magnitude of the slope indicates mainly an intermolecular solvent proton transfer to the proximal oxygen atom of the $[Cu^{II}(L_2)(OOH)]$ intermediate, producing a $[Cu^{II}(L_2)(H_2O_2)]^+$ species that rapidly releases H_2O_2 into solution. For such a reaction pathway, relatively less basic conditions are expected to favor the generation of the $[Cu^{II}(L_2)(H_2O_2)]^+$ species and, consequently, enhance the H_2O_2 production. In fact, H_2O_2 accumulation at the onset potentials increased significantly when the pH was changed from pH 9 (H_2O_2 62%) to pH 8 (H_2O_2 72%) to neutral pH 7 (H_2O_2 85%), as determined by RRDE experiments (Figure S68a). Nevertheless, the bare GC electrode showed no noticeable changes in ring current with pH variation (Figure S68b). The plot of the amount of H_2O_2 generated at different pHs for **2**$^+$ (Figure S69) demonstrates the presence of a protonation equilibrium involving the Cu^{II}-OOH species. From the sigmoidal simulation of the data, the pK_a of Cu^{II}-O(**H**)OH was estimated to be approximately 7.7. A solvent kinetic isotope effect (KIE) of ~2.24 was determined using the peak current method at neutral pH(H_2O)/pD(D_2O) conditions (Figure S70). This deuterium isotope effect indicates that solvent proton donation is involved in the rate-determining step. Notably, the observed KIE value is consistent with those reported for similar protonation steps in enzymatic systems.[85,86]

On the other hand, the ORR peak currents for **1**$^+$ did not vary with changes in pH (Figure S66a). The corresponding $\log(k_{cat})$ *vs*. pH plot (Figure S71) shows a slope of zero, indicating that the reaction rate is independent of solvent proton concentrations. This behavior apparently suggests an intramolecular proton transfer from the pendant amide N-H to the Cu^I-OOH moiety, as discussed above. In addition, the amount of the reduced oxygen products remained almost constant across the pH range from 9 to 7: pH 9, 87% H_2O and 13% H_2O_2; pH 8, 86 % H_2O and 14 % H_2O_2; pH 7, 86% H_2O and 14%

View Article Online
DOI: 10.1039/D6DT00632A

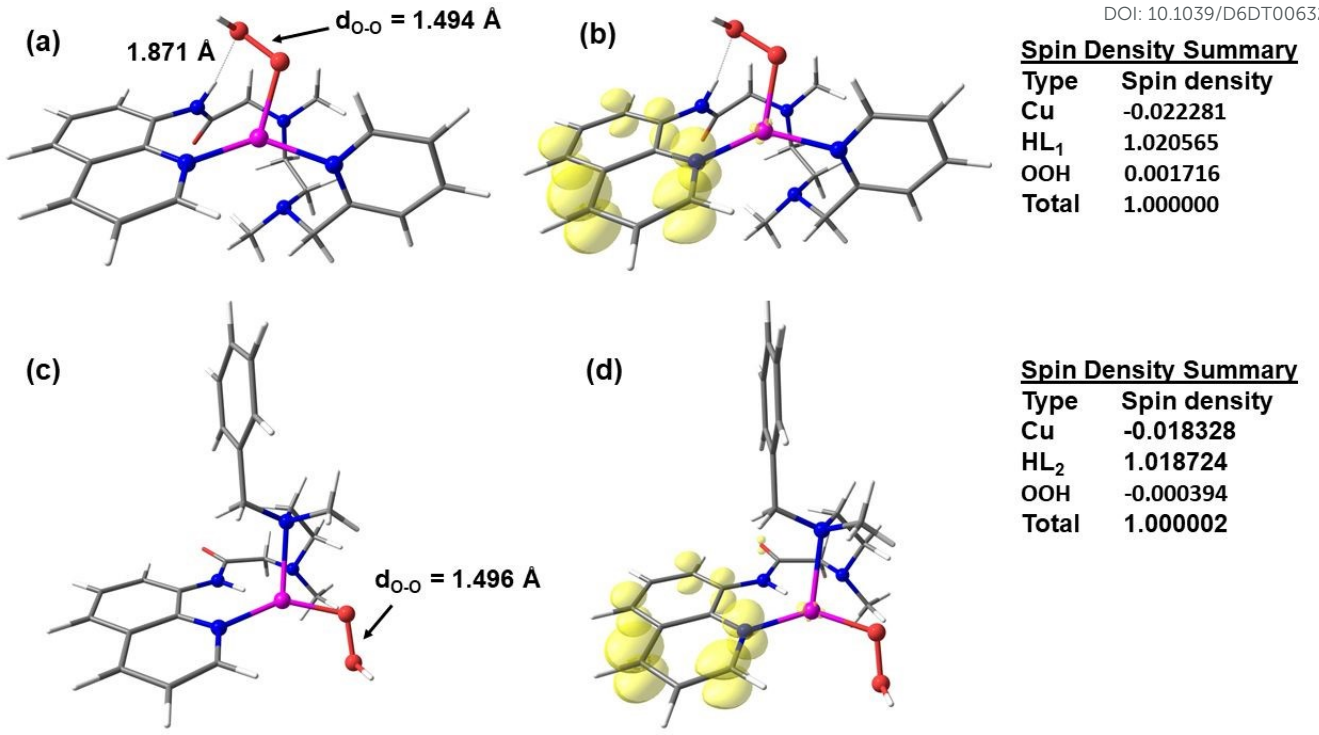

Figure 8. (a) DFT-optimized structure of the $[(HL_1^{\bullet-})Cu^{I}\text{-}OOH]^{-}$ species, and (b) the corresponding spin density plot in the doublet ground state. (c) DFT-optimized structure of the $[(HL_2^{\bullet-})Cu^{I}\text{-}OOH]^{-}$ species, and (d) the corresponding spin density plot in the doublet ground state. Color code: Cu magenta; N blue; O red; C gray; H white.

H_2O_2 (Figure S72), determined by RRDE at the onset potential. This consistency in product formation across the investigated pH range supports a localized proton-transfer mechanism that does not depend on bulk solvent protons. A KIE value of 1.05 was determined for the O_2 reduction reaction catalyzed by **1**$^+$ under neutral pH(H_2O)/pD(D_2O) conditions (Figure S73). This KIE of about 1 implies that no proton shuttle is involved in the rate-determining step. Thus, the internal proton transfer likely occurs at a relatively faster rate and is assigned as the selectivity-determining step. The rate-determining step may occur either before or after the selectivity-determining step; however, no further conclusions can be made at this point.

Previous studies by Hetterscheid *et al.* showed that ORR selectivity might also depend on the $E_{1/2}$ values of copper complexes, with more positive values favoring the overall four-electron reduction to water and more negative values favoring H_2O_2 accumulation.[67] In the present complexes, however, we observed a reversal of this expected trend. Complex **2**$^+$, which has a more positive $E_{1/2}$ (0.114 V), accumulates more H_2O_2, whereas complex **1**$^+$, with a lower $E_{1/2}$ (-0.076 V), preferentially catalyzes the complete four-electron reduction to water. This reverse selectivity based on the $E_{1/2}$ values, together with the observed pH effects, strengthens our conclusion that the nature of the proton shuttle (internal *vs.* external) plays a dominant role in determining ORR product selectivity for complexes **1**$^+$ and **2**$^+$.

Summary and Conclusions

In this work, we reported the electrocatalytic ORR activity of two Cu(II) complexes, $[Cu(L_1)]^+$ (**1**$^+$) and $[Cu(L_2)(H_2O)]^+$ (**2**$^+$), in neutral aqueous solutions. Complex **1**$^+$, supported with a penta-dentate L_1^- ligand, preferentially catalyzes the direct $4e^-/4H^+$ reduction of O_2 to H_2O over the $2e^-/2H^+$ reduction, while complex **2**$^+$, having the tetradentate ligand framework L_2^-, primarily catalyzes the $2e^-/2H^+$ reduction of O_2 to H_2O_2. The $4e^-/4H^+$ ORR rates of **1**$^+$ are pH-independent, exhibiting a solvent KIE of only 1.05 estimated at neutral pH/pD conditions. Furthermore, the RRDE experiments showed that the product distribution for ORR with **1**$^+$ remains nearly unchanged over the pH range from basic (pH 9) to neutral (pH 7). These observations suggest that the ORR of **1**$^+$ is practically unaffected by external solvent proton concentration, which endorses an internal proton transfer mechanism. Supporting this, the DFT-optimized structure of the $2e^-/H^+$ reduced form of the Cu^{II}-OOH intermediate derived from **1**$^+$ reveals a strong intramolecular H-bond between the pendant amide N-H and the distal oxygen atom of the Cu^{I}-OOH moiety. This interaction is proposed to facilitate the internal proton transfer during the reductive cleavage of O-O bond, ultimately yielding H_2O.

In contrast, the $2e^-/2H^+$ O_2 reduction rates of **2**$^+$ showed significant pH dependence, increasing as pH decreased from 9 to 7. The relative H_2O_2 production increased from 65% at pH 9 to 85% at pH 7, as determined in the RRDE experiments at the onset potential. A moderate solvent KIE of 2.24 was estimated for the $2e^-/2H^+$ O_2 reduction for **2**$^+$ at neutral conditions. The KIE of 2.24 suggests that protonation of the Cu^{II}-OOH species by an external solvent proton likely occurred in a rate-determining step of the ORR catalyzed by **2**$^+$. Analysis of the calculated structure of the $2e^-/H^+$ reduced form of

Cu^{II}-OOH, derived from the $\mathbf{2}^{+}$, discards the possibility of intramolecular proton transfer. The pendant amide N-H and the Cu^{I}-OOH moiety lie on opposite sides, precluding any effective internal proton relay and disfavoring the $4e^-$ reduction of O_2 to water.

In summary, using complexes $\mathbf{1}^{+}$ and $\mathbf{2}^{+}$, we demonstrated how internal and external proton-transfer pathways influence ORR product selectivity. Although complexes $\mathbf{1}^{+}$ and $\mathbf{2}^{+}$ exhibit larger overpotentials, the results show that a proximal proton-donor site near the reactive Cu-OOH center, capable of participating in intramolecular proton transfer, is crucial for achieving the direct $4e^-/4H^+$ reduction of dioxygen to water. However, achieving control over selectivity alone is not sufficient. Lowering the overpotential is also essential for developing energy-efficient ORR catalysts. Fine control over ligand donor strength through electronic modulation, along with the incorporation of redox-active and proton-reservoir sites, and optimization of proton relay pathways, may improve catalytic efficiency and selectivity.

Experimental Section

General. All chemicals and reagents were obtained commercially, and no further purification was performed. Organic solvents were dried before use. Phosphate buffer solutions were prepared using Milli-Q water. The synthesis of 2-chloro-*N*-(quinol-8-yl)acetamide was performed following a previously reported procedure.[87]

Synthesis of ligands. (a) The ligand 2-(methyl(2-(methyl(pyridin-2-ylmethyl)amino)ethyl)amino)-*N*-(quinolin-8-yl)acetamide (HL_1) was synthesized in a two-step procedure described below.

Step I: Synthesis of *N,N′*-dimethyl-*N*-(pyridin-2-ylmethyl)ethane-1,2-diamine. *N,N′*-dimethylethylenediamine (0.500 g, 5.672 mmol) and 2-pyridinecarboxaldehyde (0.608 g, 5.672 mmol) were dissolved in 30 mL of ethanol and stirred for one hour. After removing the solvent, the residue was dissolved in 50 mL of methanol, cooled to 0°C, and treated with two equivalents of sodium cyanoborohydride ($NaBH_3CN$). The reaction mixture was stirred at room temperature for 10 minutes, and 2 mL of trifluoroacetic acid (TFA) was added. The mixture was stirred overnight under a dinitrogen atmosphere and then quenched by adding 100 mL of 4 M sodium hydroxide. The aqueous phase was extracted twice with chloroform to separate the product. The combined organic layers were dried over anhydrous Na_2SO_4 and evaporated to obtain the desired product as an oily residue. Yield: 0.712 g, 70%. ESI(+)-MS (in methanol containing ammonium formate buffer): *m/z* 180.1547 (simulated for $C_{10}H_{18}N_3$ $[M + H]^+$: *m/z* 180.1501). ^1H NMR (400 MHz, $CDCl_3$, 300 K): δ(ppm) 8.53 (d, 1H), 7.64 (t, 1H), 7.39 (d, 1H), 7.15 (t, 1H), 3.66 (s, 2H), 2.68 (t, 2H), 2.58 (t, 2H), 2.40 (s, 3H), 2.26 (s, 3H).

Step II: Synthesis of 2-(methyl(2-(methyl(pyridin-2-ylmethyl)amino)ethyl)amino)-*N*-(quinolin-8-yl)acetamide (HL_1). In a round-bottom flask, *N,N′*-dimethyl-*N*-(pyridin-2-ylmethyl)ethane-1,2-diamine (0.600 g, 3.347 mmol) and 2-chloro-*N*-(quinol-8-yl)acetamide (0.740 g, 3.353 mmol) were taken together and dissolved in 70 mL of acetonitrile. Into this solution, *N,N*-diisopropylethylamine (DIPEA) (5.8 mL, 33.297 mmol) and potassium iodide (0.060 g) were added. The mixture was stirred and refluxed under a dinitrogen atmosphere for 72 hours. Subsequently, it was cooled to room temperature, and the solvent was removed under reduced pressure to isolate a reddish oily residue. This oily substance was purified by column chromatography on silica using CH_2Cl_2/CH_3OH as the eluent to obtain the pure reddish oily ligand. Yield: 0.815 g, 67%. ESI(+)-MS (in methanol containing ammonium formate buffer): *m/z* 364.2138 (simulated for $C_{21}H_{26}N_5O$ $[M + H]^+$: *m/z* 364.2137). ATR-FTIR (cm^{-1}, a few selected bands): 3290 (ν(N-H)$_{amide}$), 1682 (ν(C=O)$_{amide}$). ^1H NMR (400 MHz, $CDCl_3$, 300 K): δ(ppm) 11.31 (s, 1H, NH), 8.81 (d, 1H), 8.74 (d, 1H), 8.45 (d, 1H), 8.13 (d, 1H), 7.58-7.52 (m, 2H), 7.47-7.42 (m, 3H), 7.02 (t, 1H), 3.69 (s, 2H), 3.32 (s, 2H), 2.76 (s, 4H), 2.47 (s, 3H), 2.29 (s, 3H). ^{13}C NMR (125 MHz, $CDCl_3$, 300 K): δ(ppm) 169.9 (-CONH-), 159.3, 148.8, 148.3, 138.9, 136.2, 135.9, 134.4, 127.9, 127.2, 122.9, 121.8, 121.6, 121.4, 116.6, 64.2, 62.8, 55.7, 43.8 (-CH_3), 42.7 (-CH_3).

(b) The synthesis of ligand 2-((2-(benzyl(methyl)amino)ethyl)(methyl)amino)-*N*-(quinolin-8-yl)acetamide (HL_2) comprises the following two steps.

Step I: Synthesis of *N,N′*-dimethyl-*N*-benzyl-ethane-1,2-diamine. This compound was synthesized following a procedure similar to that described above for *N,N′*-dimethyl-*N*-(pyridin-2-ylmethyl)ethane-1,2-diamine, except that benzaldehyde (5.672 mmol) was added in place of 2-pyridinecarboxaldehyde in the reaction mixture. Yield: 0.750 g, 74%. ESI(+)-MS (in methanol containing ammonium formate buffer): *m/z* 179.1594 (simulated for $C_{11}H_{19}N_2$ $[M + H]^+$: *m/z* 179.1548). ^1H NMR (400 MHz, $CDCl_3$, 300 K): δ(ppm) 7.33 (s, 5H), 3.45 (s, 2H), 2.62 (t, 2H), 2.48 (t, 2H), 2.35 (s, 3H), 2.14 (s, 3H).

Step II: Synthesis of 2-((2-(benzyl(methyl)amino)ethyl)(methyl)amino)-*N*-(quinolin-8-yl)acetamide (HL_2). The ligand HL_2 was synthesized from a reaction between *N,N′*-dimethyl-*N*-benzyl-ethane-1,2-diamine (0.600 g, 3.366 mmol) and 2-chloro-*N*-(quinol-8-yl)acetamide (0.743 g, 3.366 mmol) in the presence of DIPEA and a catalytic amount of KI in acetonitrile solvent under reflux conditions for 3 days. The procedure followed was as described for the synthesis of HL_1. The pure, yellowish, oily product was isolated by column chromatography on silica gel using CH_2Cl_2/methanol as the eluent. Yield: 0.855 g, 70%. ESI(+)-MS (in methanol containing ammonium formate buffer): *m/z* 363.2198 (simulated for $C_{22}H_{27}N_4O$ $[M + H]^+$: *m/z* 363.2185). ATR-FTIR (cm^{-1}, a few selected bands): 3325 (ν(N-H)$_{amide}$), 1677 (ν(C=O)$_{amide}$). ^1H NMR (400 MHz, $CDCl_3$, 300 K): δ(ppm) 11.32 (s, 1H, NH), 8.81 (d, 1H), 8.74 (d, 1H), 8.13 (d, 1H), 7.56-7.50 (m, 2H), 7.42-7.40 (m, 1H), 7.29 (d, 2H), 7.21-7.15 (m, 3H), 3.52 (s, 2H), 3.31 (s, 2H), 2.73 (m, 4H), 2.46 (s, 3H), 2.23 (s, 3H). ^{13}C NMR (125 MHz, $CDCl_3$, 300 K): δ(ppm) 170.5 (-CONH-), 148.8, 139.5, 139.4, 136.4, 134.9, 129.4, 128.5, 127.7, 127.3, 122.0, 121.9, 117.1, 63.3, 63.2, 56.2, 55.9, 44.3 (-CH_3), 42.9 (-CH_3).

Synthesis of Cu(II) complexes.

The Cu(II) complexes with ligands HL_1 and HL_2 were synthesized using a similar procedure. The corresponding ligand (0.260 mmol) was dissolved in 15 mL of methanol. An equimolar amount of sodium methoxide was added to this solution, and the mixture was stirred for 20 minutes. Subsequently, a separate methanolic solution of $Cu^{II}(ClO_4)_2{\cdot}6H_2O$ (0.260 mmol) was added dropwise to the ligand solution. The reaction mixture was stirred for an hour at room temperature under aerobic conditions. Any insoluble materials were filtered off, and the solution volume was reduced to approximately 3 mL using a rotary evaporator. After that, excess diethyl ether was added to precipitate the complex, which was collected by filtration, washed with diethyl ether, and dried under vacuum.

[$Cu^{II}(L_1)](ClO_4)$ ($1(ClO_4)$). Yield: 0.083 g (60%). Color: green. Anal. calcd for $C_{21}H_{24}ClCuN_5O_5$: C 48.00, H 4.60, N 13.33; Found: C 47.96, H 4.52, N 13.20. ESI(+)-MS (in methanol): *m/z* 425.1263 (simulated for $C_{21}H_{24}CuN_5O$ $[Cu(L_1)]^+$: *m/z* 425.1277). ATR-FTIR (cm^{-1}, solid sample, a few selected bands): 1624 ($\nu(C{=}O)_{amide}$), 1080 & 622 ($\nu(ClO_4)$). UV-vis [λ_{max}, nm (ε, M^{-1} cm^{-1})]: (in methanol) 257 (36700), 365 (3825), 598 (87), 820 (25), 975 (sh, 15).

[$Cu^{II}(L_2)(MeOH)](ClO_4)$ ($2a(ClO_4)$). Yield: 0.100 g (69%). Color: greenish yellow. Anal. calcd for $C_{23}H_{29}ClCuN_4O_6$: C 49.64, H 5.25, N 10.07; Found: C 49.52, H 5.10, N 9.97. ESI(+)-MS (in methanol): *m/z* 424.1312 (simulated for $C_{22}H_{25}CuN_4O$ $[Cu(L_2)]^+$: *m/z* 424.1324). ATR-FTIR (cm^{-1}, solid sample, a few selected bands): 3590-3384 (br, $\nu(OH)_{methanol}$), 1601 ($\nu(C{=}O)_{amide}$), 1080 & 620 ($\nu(ClO_4)$). UV-vis [λ_{max}, nm (ε, M^{-1} cm^{-1})]: (in methanol) 257 (28590), 365 (3190), 620 (145), 930 (br, 20). Dissolving the compound in water produced *in situ* an aqua-ligated complex $[Cu^{II}(L_2)(H_2O)](ClO_4)$ (**$2(ClO_4)$**). UV-vis [λ_{max}, nm (ε, M^{-1} cm^{-1})]: (in water) 254 (30210), 348 (3980), 610 (154), 954 (br, 50).

When the complex $[Cu^{II}(L_2)(MeOH)](ClO_4)$ was charged with NaNCS, a thiocyanate-coordinated compound $[Cu^{II}(L_2)(\kappa\text{-NCS})]$ (**2b**) was isolated in crystalline form. Single crystals for X-ray crystallographic analysis were obtained by slow diffusion of diethyl ether vapor into a methanolic solution of the thiocyanate complex. ATR-FTIR (cm^{-1}, solid sample, a few selected bands): 2076 (ν(NCS)), 1618 ($\nu(C{=}O)_{amide}$). UV-vis [λ_{max}, nm (ε, M^{-1} cm^{-1})]: (in methanol) 257 (28140), 363 (3240), 632 (170), 970 (br, 80).

Synthesis of Zn(II) complexes.

The Zn(II) complexes with ligands HL_1 and HL_2 were synthesized according to the procedure described for the Cu(II) complexes; however, $Zn^{II}(ClO_4)_2{\cdot}6H_2O$ (0.260 mmol) was added instead of $Cu^{II}(ClO_4)_2{\cdot}6H_2O$ in the reaction solutions.

[$Zn^{II}(L_1)(MeOH)](ClO_4)$ ($3(ClO_4)$). Yield: 0.085 g (58%). Color: pale yellow. Anal. calcd for $C_{22}H_{28}ClN_5O_6Zn$: C 47.24, H 5.05, N 12.52; Found: C 47.14, H 4.92, N 12.28. ESI(+)-MS (in methanol): *m/z* 426.1268 (simulated for $C_{21}H_{24}N_5OZn$ $[Zn(L_1)]^+$: *m/z* 426.1272). ATR-FTIR (cm^{-1}, solid sample, a few selected bands): 3595-3420 (br, $\nu(OH)_{methanol}$), 1555 ($\nu(C{=}O)_{amide}$), 1080 & 621 ($\nu(ClO_4)$). UV-vis [λ_{max}, nm (ε, M^{-1} cm^{-1})]: (in methanol) 256 (27730), 360 (3810). ^{1}H NMR (400 MHz, CD_3OD, 300 K): δ(ppm) 9.02 (d, 1H), 8.94 (d, 1H), 8.54 (d, 1H), 8.26 (t, 1H), 8.00 (d, 1H), 7.78 (t, 1H), 7.75 (d, 1H), 7.67 (t, 1H), 7.62-7.57 (m, 2H), 3.97 (s, 2H), 3.53 (d, 1H), 3.20 (d, 1H), 3.00 (t, 1H), 2.69 (t, 1H), 2.45 (t, 2H), 2.31 (s, 3H), 1.90 (s, 3H). ^{13}C NMR (125 MHz, CD_3OD, 300 K): δ(ppm) 172.4 (-CON-), 157.2, 150.1, 147.7, 142.5, 141.6, 141.2, 140.9, 130.6, 129.9, 126.8, 126.2, 122.9, 121.2, 65.2, 60.8, 56.3, 54.2, 42.6, 42.2.

[$Zn^{II}(L_2)(MeOH)_2](ClO_4)$ ($4(ClO_4)$). Yield: 0.084 g (55%). Color: yellow. Anal. calcd for $C_{24}H_{33}ClN_4O_7Zn$: C 48.83, H 5.63, N 9.49; Found: C 48.72, H 5.35, N 9.30. ESI(+)-MS (in methanol): *m/z* 425.1317 (simulated for $C_{22}H_{25}N_4OZn$ $[Zn(L_2)]^+$: *m/z* 425.1320). ATR-FTIR (cm^{-1}, solid sample, a few selected bands): 3650-3480 (br, $\nu(OH)_{methanol}$), 1556($\nu(CO)_{amide}$), 1086 & 621 ($\nu(ClO_4)$). UV-vis [λ_{max}, nm (ε, M^{-1} cm^{-1})]: (in methanol) 253 (27890), 356 (4420). ^{1}H NMR (400 MHz, DMSO-d_6, 300 K) δ(ppm): 9.04 (d, 1H), 8.85 (d, 1H), 8.61 (d, 1H), 7.78 (dd, 1H), 7.61-7.53 (m, 2H), 7.32-7.21 (m, 5H), 3.76 (d, 1H), 3.16 (d, 1H), 3.11 (d, 1H), 2.97 (t, 1H), 2.87 (t, 1H), 2.64 (d, 1H), 2.54 (s, 3H), 2.31(d, 1H), 2.22 (d, 1H), 1.90 (s, 3H).

Author contributions

View Article Online
DOI: 10.1039/D6DT00632A

MM performed all the work reported in this paper, except for the RRDE experiments and computational studies. He also wrote the manuscript, taking input from all other authors. AG performed the DFT calculations and designed the TOC. SG conducted the RRDE experiments. SM supervised the whole project, arranged funding, and contributed to editing and correcting the manuscript.

Conflicts of interest

There are no conflicts to declare.

Data availability

The data that support the findings of this study are available in the supplementary material of this article. Deposition numbers 2454093 and 2454094 contain the supplementary crystallographic data for this paper.

Acknowledgements

MM and AG thank IIT Kharagpur for their Ph.D. fellowships. SM acknowledges the Science and Engineering Research Board (SERB) for providing funds to procure the electrochemical analyzer in his laboratory through the project EMR/2015/001136. SM also thanks the Council of Scientific and Industrial Research (project no. 01(3052)/21/EMR-II) and the Department of Chemistry at IIT Kharagpur for providing financial support for the research. The Central Research Facility and PARAM SHAKTI computing resources of IIT Kharagpur are gratefully acknowledged. The authors thank the DST-FIST program (SR/FST/CSII-026/2013) for the NMR facility at the Department of Chemistry, IIT Kharagpur. SM thanks Prof. C. Retna Raj of the Functional Materials and Electrochemistry Laboratory, Department of Chemistry, IIT Kharagpur, for providing access to the RRDE facility. MM thanks Mr. Rajib Samanta from Prof. T. K. Paine's group at IACS, Kolkata, for recording a few EPR spectra during the revision stage. MM acknowledges using Grammarly as an AI tool to correct grammar and improve the clarity of the English in his write-up.

Notes and references

1 M. Winter and R. J. Brodd, *Chem. Rev*., 2004, **104**, 4245−4269.
2 F. Cheng and J. Chen, *Chem. Soc. Rev*., 2012, **41**, 2172−2192.
3 M. L. Pegis, C. F. Wise, D. J. Martin and J. M. Mayer, *Chem. Rev*., 2018, **118**, 2340−2391.
4 H. A. Gasteiger, S. S. Kocha, B. Sompalli and F. T. Wagner, *Appl. Catal. B,* 2005, **56**, 9−35.
5 S, Dey, B. Mondal, S. Chatterjee, A. Rana, S. Amanullah and A. Dey, *Nat. Rev. Chem*., 2017, **1**, 0098.
6 S. Fukuzumi, Y.-M. Lee and W. Nam, *ChemCatChem,* 2018, **10**, 9-28.
7 S. Bhunia, A. Ghatak and A. Dey, *Chem. Rev.,* 2022, **122**, 12370-12426.
8 Y. Wang, G. I. N. Waterhouse, L. Shang and T. Zhang, *Adv. Energy Mater*., 2021, **11**, 2003323.
9 Y-T. Xi, P-J. Wei, R-C. Wang and J-G. Liu, *Chem. Commun*., 2015, **51**, 7455-7458.
10 Y. Liu, Y-Y. Wu, G-J. Lv, T. Pu, X-Q. He and L-L. Cui, *Electrochim. Acta,* 2013, **112**, 269– 278.

11 R-C. Wang, T-L. Yin, P-J. Wei and J-G. Liu, *RSC Adv*., 2015, **5**, 66487–66493.
12 P-J. Wei, G-Q. Yu, Y. Naruta and J-G. Liu, *Angew. Chem. Int. Ed*., 2014, **53**, 6659-6663.
13 I. Hijazi, T. Bourgeteau, R. Cornut, A. Morozan, A. Filoramo, J. Leroy, V. Derycke, B. Jousselme and S. Campidelli, *J. Am. Chem. Soc.,* 2014, **136**, 6348-6354.
14 H. Lei, C. Liu, Z. Wang, Z. Zhang, M. Zhang, X. Chang, W. Zhang and R. Cao, *ACS Catal.,* 2016, **6**, 6429-6437.
15 J. Meng, H. Lei, X. Li, J. Qi, W. Zhang and R. Cao, *ACS Catal*., 2019, **9**, 4551-4560.
16 Y. Hong, L. Li, B. Huang, X. Tang, W. Zhai, T. Hu, K. Yuan and Y. Chen, *Adv. Energy Mater*., 2021, **11**, 2100866.
17 P. M. Usov, B. Huffman, C. C. Epley, M. C. Kessinger, J. Zhu, W. A. Maza and A. J. Morris, *ACS Appl. Mater. Interfaces,* 2017, **9**, 33539-33543.
18 W. Schofberger, F. Faschinger, S. Chattopadhyay, S. Bhakta, B. Mondal, J. A. A. W. Elemans, S. Mullegger, S. Tebi, R. Koch, F. Klappenberger, M. Paszkiewicz, J. V. Barth, E. Rauls, H. Aldahhak, W. G. Schmidt and A. Dey, *Angew. Chem. Int. Ed.,* 2016, **55**, 2350-2355.
19 G. Passard, D. K. Dogutan, M. Qiu, C. Costentin and D. G. Nocera, *ACS Catal*., 2018, **8**, 8671-8679.
20 S. Chatterjee, K. Sengupta, S. Samanta, P. K. Das and A. Dey, *Inorg. Chem.,* 2015, **54**, 2383-2392.
21 S. Chatterjee, K. Sengupta, B. Mondal, S. Dey and A. Dey, *Acc. Chem. Res.,* 2017, **50**, 1744-1753.
22 S. Bhunia, A. Rana, P. Roy, D. J. Martin, M. L. Pegis, B. Roy and A. Dey, *J. Am. Chem. Soc.,* 2018, **140**, 9444−9457.
23 A. Ghatak, S. Bhunia and A. Dey, *ACS Catal*., 2020, **10**, 13136-13148.
24 B. D. Matson, C. T. Carver, A. V. Ruden, J. Y. Yang, S. Raugei and J. M. Mayer, *Chem. Commun*., 2012, **48**, 11100–11102.
25 C. T. Carver, B. D. Matson and J. M. Mayer, *J. Am. Chem. Soc*., 2012, **134**, 5444-5447.
26 M. L. Pegis, D. J. Martin, C. F. Wise, A. C. Brezny, S. I. Johnson, L. E. Johnson, N. Kumar, S. Raugei and J. M. Mayer, *J. Am. Chem. Soc*., 2019, **141**, 8315-8326.
27 X. Lu, Y-M. Lee, M. Sankaralingam, S. Fukuzumi and W. Nam, *Inorg. Chem*., 2020, **59**, 18010-18017.
28 S. Fukuzumi, K. Okamoto, C. P. Gros and R. Guilard, *J. Am. Chem. Soc*., 2004, **126**, 10441-10449.
29 K. M. Kadish, L. Fremond, J. Shen, P. Chen, K. Ohkubo, S. Fukuzumi, M. E. Ojaimi, C. P. Gros, J-M. Barbe and R. Guilard, *Inorg. Chem*., 2009, **48**, 2571-2582.
30 R. Jr. McGuire, D. K. Dogutan, T. S. Teets, J. Suntivich, Y. Shao-Horn and D. G. Nocera, *Chem. Sci*., 2010, **1**, 411–414.
31 A. Schechter, M. Stanevsky, A. Mahammed and Z. Gross, *Inorg. Chem.,* 2012, **51**, 22-24.
32 T. Honda, T. Kojima and S. Fukuzumi, *J. Am. Chem. Soc.,* 2012, **134**, 4196−4206.
33 K. Mase, K. Ohkubo and S. Fukuzumi, *J. Am. Chem. Soc.,* 2013, **135**, 2800−2808.
34 Y. Liu, G. Zhou, Z. Zhang, H. Lei, Z. Yao, J. Li, J. Lin and R. Cao, *Chem. Sci*., 2020, **11**, 87-96.
35 H. Qin, J. Kong, X. Peng, Z. Wang, X. Li, H. Lei, W. Zhang and R. Cao, *ChemSusChem*, 2025, **18**, e202401739.
36 T. Liu, J. Meng, H. Qin, M. Zhang, N. Sun, B. Mei, H. Li, X.-P. Zhang, J. Li and R. Cao, *J. Am. Chem. Soc*., 2025, **147**, 22322-22328.
37 X. Li, X. Jin, Y. Cao, J. Zhu, D. Duan, Q. Luo, B. Lv, Y. Xu, Y. Zheng, W. Zhang, R. Long, L. Zhang, R. Liao and R. Cao, *J. Am. Chem. Soc*., 2025, **147**, 43199-43205.
38 H. Qin, Y. Wang, T. Liu, Y. Xu, H. Lei, X. Li, W. Zhang, S. Fukuzumi, W. Nam and R. Cao, *J. Am. Chem. Soc*., 2026, **148**, 933-943.
39 M. Gennari, D. Brazzolotto, J. Pecaut, M. V. Cherrier, C. J. Pollock, S. DeBeer, M. Retegan, D. A. Pantazis, F. Neese, M. Rouzieres, R. Clerac and C. Duboc, *J. Am. Chem. Soc*., 2015, **137**, 8644-8653.
40 S. L. Hooe, A. L. Rheingold and C. W. Machan, *J. Am. Chem. Soc*., 2018, **140**, 3232−3241.
41 S. L. Hooe and C. W. Machan, *J. Am. Chem. Soc*., 2019, **141**, 4379-4387.
42 L. Wang, M. Gennari, F. G. C. Reinhard, J. Gutierrez, A. Morozan, C. Philouze, S. Demeshko, V. Artero, F. Meyer, S. P. de. Visser and C. Duboc, *J. Am. Chem. Soc*., 2019, **141**, 8244-8253.
43 E. N. Cook, D. A. Dickie and C. W. Machan, *J. Am. Chem. Soc*., 2021, **143**, 16411-16418.
44 E. N. Cook, S. L. Hooe, D. A. Dickie and C. W. Machan, *Inorg. Chem*., 2022, **61**, 8387-8392.
45 A. Santra, A. Das and S. Paria, *Chem. Sci*., 2024, **15**, 4095-4105.
46 S. Fukuzumi, S. Mandal, K. Mase, K. Ohkubo, H. Park, J. Benet-Buchholz, W. Nam and A. Llobet, *J. Am. Chem. Soc.,* 2012, **134**, 9906-9909.
47 I. Monte-Perez, S. Kundu, A. Chandra, K. E. Craigo, P. Chernev, U. Kuhlmann, H. Dau, P. Hildebrandt, C. Greco, C. V. Stappen, N. Lehnert and K. Ray, *J. Am. Chem. Soc*., 2017, **139**, 15033-15042.
48 Y-H. Wang, M. L. Pegis, J. M. Mayer and S. S. Stahl, *J. Am. Chem. Soc*., 2017, **139**, 16458-16461.
49 A. Das, A. Ali, G. Gupta, A. Santra, P. Jain, P. P. Ingole, S. Paul and S. Paria, *ACS Catal*., 2023, **13**, 5285-5297.
50 Y-S. Tsai, Y-W. Chen, C. L. Dayawansa, H. Chang, W-C. Chen, J-S. Shen, T-G. Ong, G. P. A. Yap and V. C.-C. Wang, *Inorg. Chem*., 2025, **64**, 4213-4222.
51 J. Y. Yang, R. M. Bullock, W. G. Dougherty, W. S. Kassel, B. Twamley, D. L. DuBois and M. R. DuBois, *Dalton Trans*., 2010, **39**, 3001-3010.
52 S. Realista, P. Ramgi, B. de P. Cardoso, A. I. Melato, A. S. Viana, M. J. Calhorda and P. N. Martinho, *Dalton Trans*., 2016, **45**, 14725–14733.
53 S. Fukuzumi, H. Kotani, H. R. Lucas, K. Doi, T. Suenobu, R. L. Peterson and K. D. Karlin, *J. Am. Chem. Soc*., 2010, **132**, 6874-6875.
54 L. Tahsini, H. Kotani, Y-M. Lee, J. Cho, W. Nam, K. D. Karlin, and S. Fukuzumi, *Chem. Eur. J*., 2012, **18**, 1084-1093.
55 D. Das, Y-M. Lee, K. Ohkubo, W. Nam, K. D. Karlin and S. Fukuzumi, *J. Am. Chem. Soc*., 2013, **135**, 2825-2834.
56 S. Kakuda, R. L. Peterson, K. Ohkubo, K. D. Karlin and S. Fukuzumi, *J. Am. Chem. Soc*., 2013, **135**, 6513-6522.
57 M. A. Thorseth, C. E. Tornow, E. C. M. Tse and A. A. Gewirth, *Coord. Chem. Rev*., 2013, **257**, 130-139.
58 H. Kotani, T. Yagi, T. Ishizuka and T. Kojima, *Chem. Commun*., 2015, **51**, 13385—13388.
59 C. Liu, H. Lei, Z. Zhang, F. Chen and R. Cao, *Chem. Commun*., 2017, **53**, 3189-3192.
60 M. Langerman and D. G. H. Hetterscheid, *Angew. Chem. Int. Ed*., 2019, **58**, 12974-12978.
61 N. W. G. Smits, B. van Dijk, I. de Bruin, S. L. T. Groeneveld, M. A. Siegler and D. G. H. Hetterscheid, *Inorg. Chem*., 2020, **59**, 16398-16409.
62 S. N. Chowdhury, S. Biswas, P. Das, S. Paul and A. N. Biswas, *Inorg. Chem*., 2020, **59**, 14012-14022.
63 A. Ali, D. Prakash, P. Majumder, S. Ghosh and A. Dutta, *ACS Catal*., 2021, **11**, 5934-5941.
64 M. L. Skavenborg, M. S. Moller, C. J. Miller, J. Hjelm, T. D. Waite and C. J. McKenzie, *Inorg. Chem*., 2023, **62**, 18219-18227.
65 A. Das, S. N. Chowdhury, S. Biswas, R. Samanta, A. N. Biswas and T. K. Paine, *Inorg. Chem*., 2025, **64**, 4983-4995.
66 S. Chaudhary and R. Murugavel, *Dalton Trans*., 2026, **55**, 1306-1317.

View Article Online
DOI: 10.1039/D6DT00632A

67 M. Langerman, P. H. van Langevelde, J. J. van de Vijver, M. A. Siegler and D. G. H. Hetterscheid, *Inorg. Chem*., 2023, **62**, 19593-19602.
68 V. R. I. Kaila, M. I. Verkhovsky and M. Wikstrom, *Chem. Rev*., 2010, **110**, 7062-7081.
69 S. Yoshikawa and A. Shimada, *Chem. Rev*., 2015, **115**, 1936-1989.
70 M. Fernandez-Fernandez, M. A. Sanroman and D. Moldes, *Biotechnol. Adv*., 2013, **31**, 1808-1825.
71 E. I. Solomon, D. E. Heppner, E. M. Johnston, J. W. Ginsbach, J. Cirera, M. Qayyum, M. T. Kieber-Emmons, C. H. Kjaergaard, R. G. Hadt and L. Tian, *Chem. Rev*., 2014, **114**, 3659-3853.
72 S. Stoll and A. Schweiger, *J. Magn. Reson*., 2006, **178**, 42-55.
73 S. Stoll and R. D. Britt, *Phys. Chem. Chem. Phys*., 2009, **11**, 6614-6625.
74 B. J. Hathaway, Comprehensive Coordination Chemistry, The Synthesis, Reactions, Properties and Applications of Coordination Compounds, eds. G. Wilkinson, R. D. Gillard, J. A. McCleverty, Pergamon, Oxford 1987, vol. **5**, pp. 533-774.
75 S. Roy, P. Mitra and A. K. Patra, *Inorg. Chim. Acta*., 2011, **370**, 247-253.
76 W. A. Alves, S. A. de Almeida-Filho, R. H. de A. Santos, A. Paduan-Filho and A. M. da C. Ferreira, *J. Braz. Chem. Soc*., 2004, **15**, 872-883.
77 A. W. Addison, T. N. Rao, J. Reedijk, J. V. Rijn and G. C. Verschoor, *J. Chem. Soc., Dalton Trans*., 1984, 1349-1356.
78 P. Sharrock and M. Melnik, *Can. J. Chem*., 1985, **63**, 52-56.
79 D. Kivelson and R. Neiman, *J. Chem. Phys*., 1961, **35**, 149-155.
80 M. Lefevre and J.-P. Dodelet, *Electrochim. Acta,* 2003, **48**, 2749-2760.
81 C. Costentin, S. Drouet, M. Robert and J-M. Saveant, *J. Am. Chem. Soc*., 2012, **134**, 11235-11242.
82 C. Costentin and J-M. Saveant, *ChemElectroChem,* 2014, **1**, 1226-1236.
83 J. E. Leffler, *Science,* 1953, **117**, 340-341.
84 S. Bhunia, A. Rana, S. Hematian, K. D. Karlin and A. Dey, *Inorg. Chem*., 2021, **60**, 13876-13887.
85 J. Aikens and S. G. Sligar, *J. Am. Chem. Soc.,* 1994, **116**, 1143-1144.
86 V. W. Huang, J. P. Emerson and D. M. Kurtz, *Biochemistry,* 2007, **46**, 11342−11351.
87 G. J. Stasiuk, F. Minuzzi, M. Sae-Heng, C. Rivas, H-P. Juretschke, L. Piemonti, P. R. Allegrini, D. Laurent, A. R. Duckworth, A. Beeby, G. A. Rutter and N. J. Long, *Chem. Eur. J*., 2015, **21**, 5023-5033.

Data Availability Statement

View Article Online
DOI: 10.1039/D6DT00632A

The data that support the findings of this study are available in the supplementary material of this article. Deposition numbers 2454093 and 2454094 contain the supplementary crystallographic data for this paper.